



Arsenic-poor fluids promote strong As partitioning into pyrite

Martin Kutzschbach^{a,*}, Frederik Dunkel^a, Christof Kusebauch^b, Ferry Schipperski^a,
Frederik Börner^c, Henrik Drake^d, Kevin Klimm^e, Manuel Keith^c

^a Technische Universität Berlin, Applied Geochemistry, Berlin, Germany

^b GFZ German Research Centre for Geosciences, Potsdam, Germany

^c Friedrich-Alexander-Universität (FAU) Erlangen-Nürnberg, GeoZentrum Nordbayern, Erlangen, Germany

^d Department of Biology and Environmental Science, Linnaeus University, Kalmar, Sweden

^e Goethe-Universität Frankfurt, Institut für Geowissenschaften, Frankfurt am Main, Germany

ARTICLE INFO

Associate editor: Georges Calas

Keywords:

Arsenic partitioning
Pyrite
Siderite
Geothermal energy
Ore deposits
Groundwater remediation
Hydrothermal systems

ABSTRACT

Pyrite is a ubiquitous sulfide mineral found in diverse geological settings and holds great significance in the formation of Au deposits as well as the safe utilization of groundwater due to its remarkable ability to incorporate substantial amounts of As. However, despite its importance, there remains a dearth of fundamental data on the partitioning of As between pyrite and fluid, which is key for accurately modeling the As distribution in these environments.

Here, we present new insights into the partitioning behavior of As between pyrite and fluid at conditions that mimic natural fluid systems. Pyrite was synthesized by replacement of natural siderite in hydrothermal experiments at 200 °C and pH 5 applying a wide range of fluid As concentrations, spanning from 0.001 to 100 µg/g. The As distribution and concentration in synthetic pyrite was analyzed by quantitative LA-ICP-MS mapping providing a high spatial resolution and sensitivity at 2–3 µm image pixel size at a detection limit of ~1 µg/g at the single pixel scale. Pyrite-fluid partitioning coefficients ($D_{As}^{(py/fluid)}$) between synthetic pyrite and experimental fluid agree with previously published data for high fluid As concentrations of 1 µg/g to 100 µg/g ($D_{As} < 2000$). However, at low As concentrations in the experimental fluid (<1 µg/g), a steep increase in the $D_{As}^{(py/fluid)}$ values of up to ~30,000 was detected, demonstrating even stronger As partitioning into pyrite. This is confirmed by the analyses of natural pyrite that precipitated from As-poor fluids (0.3–0.4 ng/g) within a deep anoxic aquifer in SE Sweden. The discovery holds significant implications for the mobility and scavenging of As, which in turn is important for understanding the formation and fingerprinting of mineral deposits as well as for the secure utilization of groundwater resources.

1. Introduction

Pyrite (FeS₂) is the most common sulfide mineral in hydrothermal systems of the Earth's crust, which is due to its stability over a wide range of pH (0–9), temperature (up to 740 °C) and redox conditions (Nordstrom, 1982; Evangelou, 1995; Craig et al., 1998; Kusebauch et al., 2018). In combination with its ability to incorporate various trace elements (such as As, Ag, Au, Cu, Ni, Co, Pb, Sb, Se, Te) either through solid solution or as micro- to nano-scale inclusions, this makes pyrite a valuable tracer for comprehending hydrothermal (ore-forming) systems (Keith et al., 2018; Ciobanu et al., 2012; Deditius et al., 2011; Large et al., 2009; Palenik et al., 2004; Mukherjee and Large, 2016; Reich et al., 2013).

Arsenic has variable oxidation states (–1, +2, +3, +5), and can substitute for both Fe and S in the crystal lattice of pyrite (Deditius et al., 2008; Keith et al., 2018). Arsenic-rich ('arsenian') pyrite that commonly forms from reduced hydrothermal fluids, as known from Carlin-type and some epithermal deposits, mostly hosts As[–], which substitutes for S[–] in the pyrite structure (Simmons et al., 2005; Deditius et al., 2014; Keith et al., 2018). The preferred incorporation of As[–] into pyrite from rather reduced fluids is confirmed by high pyrite-fluid partitioning coefficients $D_{As}^{(py/fluid)}$ (300–1700) for fluids with >1 µg/g As (Reich et al., 2005; Su et al., 2008, 2009, 2012; Qian et al., 2013; Large et al., 2016; Kusebauch et al., 2018). In this context, it has been shown that As enhances the solubility of Au in the pyrite lattice, in economic Carlin-type and some epithermal deposits (Pals et al., 2003; Palenik et al., 2004; Reich et al.,

* Corresponding author.

E-mail address: m.kutzschbach@tu-berlin.de (M. Kutzschbach).

<https://doi.org/10.1016/j.gca.2024.05.027>

Received 21 February 2024; Accepted 25 May 2024

Available online 28 May 2024

0016-7037/© 2024 The Author(s). Published by Elsevier Ltd. This is an open access article under the CC BY-NC license (<http://creativecommons.org/licenses/by-nc/4.0/>).

2005; Deditius et al., 2014; Kusebauch et al., 2019; Pokrovski et al., 2019, 2021). Pyrite can host between 6 and 10 wt % of As in solid solution, whereas randomly distributed arsenopyrite domains were reported in pyrite with higher As contents (Reich and Becker, 2006; Blanchard et al., 2007; Simmons et al., 2005). Accordingly, Börner et al. (2021) recently demonstrated that the general assumption of increasing Au with increasing As in pyrite is only valid for As contents <13 wt %, whereas decreasing Au contents were reported above this threshold.

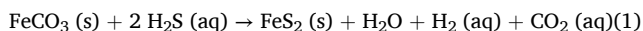
Beyond the economic interest of using As in pyrite as a vector towards Au-rich mineralization, it also poses a latent risk, as As can be released during pyrite dissolution under more oxidizing conditions eventually induced artificially through aquifer storage and recovery (Jones and Pichler, 2003; Stuyfzand and Bonte, 2023) or geothermal energy production (Burnside et al., 2016). In addition, high levels of As in pyrite are a primary cause of alarmingly high As concentrations in groundwater and running water associated with active or abandoned mining and in industrial areas (Baragaño et al., 2020; Oliveira et al., 2012; Savage et al., 2000). Even low levels of As in the range of 10 µg/l in groundwater can be considered as a potential health risk, and are observed in many developing countries (Smith and Smith, 2004).

Hence, despite the critical importance of understanding how As is incorporated in pyrite from fluids to constrain the sources of groundwater As contamination and to reconstruct the ore-forming processes of precious metal deposits, there is currently a lack of systematically derived $D_{As}^{(py/fluid)}$ data at As levels below 1 µg/g, which are known from natural and artificial (geothermal) pyrite-forming hydrothermal environments (Drake et al., 2015; Schmidt et al., 2017). The availability of such data would be particularly beneficial for modeling As mobility in subsurface hydrothermal systems or during fluid-rock interaction to better constrain the formation conditions of As-rich pyrite in the context of ore formation and environmental As pollution. To address these knowledge gaps, hydrothermal experiments were conducted under reduced fluid conditions ($-43.9 \log fO_2$), where pyrite replaced precursor siderite by interaction with fluids of variable As concentration (0001–100 µg/g).

2. Methods and experimental materials

2.1. Hydrothermal synthesis and starting materials

Pyrite was synthesized following Kusebauch et al. (2018) via hydrothermal replacement of natural siderite (FeCO₃) at 200 °C and pH 5 in H₂S-bearing solutions via the reaction:



Experiments were carried out in large volume (50 ml) PTFE-lined stainless-steel autoclaves to achieve high fluid/solid ratios (~6000), while still obtaining sufficiently sized pyrite grains for convenient in situ chemical analysis. The large fluid reservoir was chosen to maintain constant As concentrations in the fluid throughout the experiments. The following starting materials were used:

- (1) Siderite (FeCO₃): The siderite used in this study originates from a cryolite deposit in Ivigtut, Greenland. A euhedral crystal of approximately 3.5 cm³ was crushed and the size fraction of 250–500 µm was separated by sieving. Individual crystal fragments were mostly transparent, occasionally displaying thin (<10 µm) brown limonite coatings on cleavage planes and crystal faces (Fig. S1). The siderite is homogeneous and depicts near end-member composition with minor amounts of Mn (Fe_{0.96(1)}Mn_{0.04(1)}CO₃), which agrees with published siderite data from Ivigtut (Sliwinski et al., 2018). Trace element analysis by LA-ICP-MS (cf. Section 2.4.4) revealed As concentrations below the minimum detection limit of 0.02 µg/g in clear parts of the siderite crystal (Table S1). The limonite coatings show detectable, but negligible

amounts of As (<1 µg/g, Fig. S1b). About 20–30 clear siderite grains (~5 mg) without coating (Fig. S1) were handpicked for each experiment.

- (2) Thioacetamid (C₂H₅NS): Solid thioacetamide (Sigma-Aldrich) is highly soluble in aqueous solutions and decomposes to ammonium acetate and hydrogen sulfide when heated, which served as the S donor for pyrite synthesis (Qian et al., 2013; Kusebauch et al., 2018, 2019). Approximately 96 mg solid thioacetamide were weighed into each PTFE beaker. This results in an H₂S concentration of 0.043 mol/l, assuming complete decomposition of thioacetamide to ammonium acetate and hydrogen sulfide.
- (3) pH-buffer: A sodium acetate/acetic acid buffer at pH 5 (Sigma-Aldrich) was used for all experimental runs. Two buffer solutions at high and low concentrations were prepared (Table 1). After verifying the pH values with a pH probe, 25 ml of the buffer solution were pipetted into each PTFE beaker. Both buffer solutions maintained the pH during the experiments, but the higher concentrated buffer showed a better performance, as indicated by a pH decrease of less than 0.06 pH units compared 0.54 pH units when using the lower buffer concentration.
- (4) Arsenic solution: Stock solutions of varying As concentrations were prepared from a NIST traceable 1000 µg/g As ICP-MS single element standard (Sigma-Aldrich). Subsequently, 5 ml of the stock solution were loaded into the beaker resulting in final fluid As concentrations of 0.001, 0.01, 0.1, 1, 10, and 100 µg/g. The filled PTFE beakers were weighed, and transferred into stainless-steel autoclaves, which were closed firmly via a screw cap. The assembly was placed in a muffle furnace at 200 °C for 168h. In a series of As-free test runs using the 250–500 µm siderite size fraction, no siderite was detected in the run products after 168h, as determined through powder X-ray diffraction (XRD) analysis. Based on these findings, a run duration of 168 h was selected for the subsequent experiments. Each sealed PTFE beaker was weighed before opening. A negligible weight loss of ~1 % was observed for all experimental runs, which indicates that all autoclaves remained airtight throughout the experiment. The pH value of the fluid was re-measured, indicating constant pH conditions over the run duration (Table 1).

2.2. Fluid and solid sample extraction and cleaning procedure

The experimental fluid from the PTFE beakers was carefully pipetted into 50 ml volumetric flasks. The beakers containing the solid run products were rinsed in a two steps procedure by (1) a few ml of 1 % concentrated nitric acid (Merck Suprapure®) and (2) ultrapure (UP) H₂O from an Arium pro VF ultrapure water system (Sartorius; 0.055 µS cm⁻¹). Rinse solutions were transferred to the volumetric flask that contained the experimental fluid and filled up with ultrapure water to achieve a total volume of 50 ml. Finally, the sample solution was filtered through a 0.45 µm syringe filter. The solid residues in the PTFE beakers were dried in an oven at 50 °C for about 24h. A 50 % fraction of the solid sample material from three experimental runs was analyzed by XRD (cf. Section 2.4.3). Crystals from the dried solid residues were embedded in 1-inch epoxy mounts and polished for subsequent analysis by Electron Probe Micro Analysis (EPMA) and Laser Ablation Inductively Coupled Plasma Mass Spectrometry (LA-ICP-MS). After each experimental run, the PTFE beakers were carefully cleaned mechanically and chemically (10 % HNO₃ for at least 24 h) to prevent As contamination.

2.3. Natural groundwater and pyrite from the Äspö hard-rock laboratory

The Swedish Nuclear Fuel and Waste Management Co. (SKB) operates a full-scale test facility in SE Sweden (Äspö Hard Rock Laboratory). Two boreholes (labeled KA3105A and KA3385A, Drake et al., 2015) were drilled horizontally at 415 and 445 m crustal depth between 1994

Table 1
Overview of pyrite synthesis experiments.

Exp. #	Initial fluid	Buffer (per 250 ml H ₂ O)		pH		initial siderite mass (mg)	w/r	final As _{fluid} (µg/g)	RSD (%)	Product phases (wt %)
	As (µg/g)	acetic acid (ml)	Na-acetat (mg)	initial	final					
V3.1	0.001	12.91	43.5	4.93	4.93	5.123	5856	0.0019	13.6	py (47) sd (21) pyh (19) mrc (13)
V3.2	0.001	12.91	43.5	4.93	4.93	5.089	5895	0.0017	19.4	py (56) pyh (24) sd (16) mrc (4)
V3.3	0.001	12.91	43.5	4.93	4.93	5.110	5871	0.0019	6.5	sd (32) py (32) mrc (20) pyh (11)
V1.5	0.01	12.91	43.5	4.96	4.98	5.160	5814	0.0106	8.7	mrc (36) py (34) pyh (16) sd (13)
V1.6	0.01	12.91	43.5	4.96	4.92	5.136	5841	0.0072	9.7	sd (54) py (35) mrc (4) pyh (8)
V1.7	0.01	12.91	43.5	4.96	4.92	4.994	6007	0.0054	17.4	sd (37) mrc (32) py (18) pyh (5) qz (8)
V2.1	0.1	12.91	43.5	4.95	4.89	5.126	5853	0.0673	7.4	sd (45) py (37) pyh (10) mrc (6) aso (tr)
V2.2	0.1	12.91	43.5	4.95	4.91	4.993	6008	0.0936	9.9	sd (85) mrc (8) py (7) mag (tr)
V2.3	0.1	12.91	43.5	4.95	4.89	5.054	5936	0.0855	2.9	sd (85) pyh (7) py (6) hem (tr)
V2.5	0.1	12.91	43.5	4.95	4.9	5.064	5924	0.0824	3.7	sd (90) mrc (5) py (4) pyh (tr)
V4.1	1	0.86	3.18	4.89	4.93	5.126	5853	0.99	1.0	py (60) hem (24) mrc (11) szo (6)
V4.2	1	0.86	3.18	4.89	4.89	5.054	5936	0.97	1.3	mrc (42) py (32) grg (15) mag (6) hem (4)
V4.3	1	0.86	3.18	4.89	4.85	5.200	5769	0.75	1.7	mrc (66) py (29) mln (5)
V4.4	1	0.86	3.18	4.89	4.82	5.044	5948	1.07	1.0	mrc (49) py (39) mln (6) mkw (4)
V5.6	1	0.86	3.18	4.87	4.94	5.124	5855	1.238	0.7	mrc (41) py (34) mln (16) hem (7) aso, mkw (tr)
V1.3	10	12.91	43.5	4.96	4.92	5.156	5818	9.866	9.4	sd (53) py (27) mrc (15) pyh (4)
V5.7	10	0.86	3.18	4.87	4.89	5.061	5928	7.805	0.7	mrc (45) py (42) hem (7) mln (6)
V4.5	100	0.86	3.18	4.89	4.4	5.166	5807	2.12	1.6	py (57) hem (19) mrc (13) grg (10)
V4.6	100	0.86	3.18	4.89	4.39	5.247	5718	2.31	1.8	py (71) hem (13) grg (10) sd (4) mrc (3)
V4.7	100	0.86	3.18	4.89	4.38	5.190	5780	2.15	2.9	py (47) grg (25) sd (15) mck (8) mln (6)
V4.8	100	0.86	3.18	4.89	4.35	5.124	5855	2.51	2.7	sd (47) py (35) grg (19)

To all experiments 96 mg of thioacetamide have been added (see methods section).

w/r = water to rock ratio based on the amount of siderite and total fluid volume of 30 ml assuming a density of 1 g/cm³.

As_{fluid} determined by ICP-MS (see methods section). RSD = internal measurement uncertainty expressed as the relative standard deviation based on the measurement of 3–5 replicates.

sd: siderite (FeCO₃); py: pyrite (FeS₂); mrc: marcasite (FeS₂); pyh: pyrrhotite (Fe_(1-x)S); grg: greigite (Fe₃S₄); mkw: mackinawite (FeS); qz: quartz (SiO₂); hem: hematite (Fe₂O₃); mag: magnetite (Fe₃O₄); mln: melanterite (Fe(H₂O)₆SO₄) • H₂O; aso: arsenolite (As₂O₃); szo: szomolnokite (FeSO₄•H₂O).

Phase content determined by XRD (see methods section). Sum of quantitative phase content may deviate from 100 wt % due to rounding. “tr” refers to phases with contents ≤ 1 wt %.

and 1995. Different borehole sections were isolated by inflatable packers. Groundwater was constantly supplied to the packed-off borehole sections by intersecting bedrock fractures. An Al-rod ran through all packer sections and groundwater was sampled in the tunnel environment by opening valves that allowed the relatively over-pressured water from the sections to pass through polyamide tubings attached to each packer. The temperature was constant at 14 °C and the pH-value was stable between 7.4 and 7.7. The borehole instrumentation was retrieved after 17 years and calcite, barite, and pyrite were scraped off the instrumentation and sampled in nitrogen-filled gas-tight bags to prevent oxidation. The chemical composition of the groundwater and of pyrite from one section of each of the boreholes are presented in this study. For more information about the site and sampling procedure see Drake et al. (2015).

2.4. Analytical methods for characterization of solid run products and natural pyrite

2.4.1. Micro X-ray fluorescence (µ-XRF)

The composition and distribution of major elements in the initial siderite was determined through µ-XRF mapping using a Bruker M4 Tornado at the MAGMA Lab of the TU Berlin. The instrument is equipped with an X-ray focusing capillary optic and two 30 mm² silicon drift detectors. Mappings were performed on a polished 1-inch epoxy mount using a 20 µm spot size. The Rh-anode operated in an evacuated chamber at 20 mbar with an acceleration voltage 50 kV and an anode current of 600 mA. Spots were set at intervals of 50 µm and measured for 200 ms. Siderite stoichiometry was derived by integrating the signal of a representative region of individual grains, which was processed to quantify relevant cations by a standardless method (Flude et al., 2017; Table S1). Concentrations of C and O were derived mathematically

assuming one CO₃ anion per formula unit.

2.4.2. Electron Probe Micro-Analysis (EPMA)

Electron back-scattered images, and major and minor element compositions of the solid run products were acquired using a JXA8200 Superprobe at the GeoZentrum Nordbayern. The measurements were performed in an evacuated chamber (<4.0 × 10⁻⁶ mbar) with a focused beam, an acceleration voltage of 20 kV and a beam current of 50 nA. The following standards were used for the quantitative analysis: FeS₂ for Fe and S, FeAsS for As, MnSiO₃ for Mn, and CaCO₃ for Ca. Data was acquired based on the following x-ray lines, spectroscopic crystals, and count times (in sec.) at the peak and background (lower and upper) positions: Fe (Kα, LIF, 20, 10, 10); S (Kα, PETJ, 20, 10, 10); As (Lα, TAP, 100, 50, 50); Mn (Kα, PETH, 100, 50, 50); Ca (Kα, PETJ, 20, 10, 10). Calculated theoretical minimum detection limits are 18 µg/g (Fe), 43 µg/g (S), 115 µg/g (Mn), 23 µg/g (Ca) and 61 µg/g (As). However, the method detection limit for As appears to be somewhat higher (~300 µg/g; see Section 3.2).

2.4.3. Powder X-ray diffraction (XRD)

Aliquots of the run products (~1–3 mg) from all experiments were analyzed using a Rigaku SmartLab XRD at the MAGMA Lab of the TU Berlin. The instrument is equipped with a copper X-ray tube. For the analysis, the run products were powdered using an agate mortar and evenly distributed on a silicon monocrystal. Measurements were conducted between 2θ = 5–80° with a step size of 0.01° and a scan speed of 10° per minute, while rotating the sample with 20 revolutions per minute. Phase identification on the resulting spectra was performed using the PDF4 database (ICDD), integrated in the Smartlab Studio II software (Rigaku). Rietveld analysis was employed to quantify the mineral phase contents, beginning with the most prominent phases

(fitted properties: background, absolute x-shift, phase scale, lattice parameters, profile function, texture).

2.4.4. Micro-Raman

Micro-Raman Spectroscopy was performed using a WITec alpha 300 R Raman imaging microscope equipped with a green laser (532nm) at the Goethe-University of Frankfurt. The system was calibrated using the 520 cm^{-1} band of silicon wafer. Spectra were collected using a 1800 g/mm grating and a 100 \times objective in the range of 130–1300 cm^{-1} with a spectral resolution of 1.3 cm^{-1} and a laser spot size of $\sim 2 \mu\text{m}$. The laser power was set to 1 mW in order to avoid any beam damage on the sample. Integration time was 5 s with 10 accumulations resulting in a total acquisition time of 50 s for each spectrum. Higher laser power of 5mW oxidised the sulfides and magnetites in the samples as indicated by the presence of hematite in the Raman-signal. All spectra were background corrected and normalised to 1 for the most intense band in the spectra.

2.4.5. Laser Ablation Inductively Coupled Plasma Mass Spectrometry (LA-ICP-MS)

Quantitative trace element mapping was performed on the run products by LA-ICP-MS during three analytical sessions (S1, S2, S3) at the MAGMA Lab of the TU Berlin, using an Agilent 8900 ICP-MS/MS coupled to an Analyte Excite 193 nm excimer laser (Teledyne Photon Machines). The aerosol rapid introduction system ARIS (Teledyne Photon Machines) was used in combination with a low-volume adapter from Glass Expansion. Helium (99.999 %) was used as a carrier gas with a total flow rate of 0.95 l/min (0.5 l/min cell flow, 0.45 l/min cup flow). After plasma ignition and initialization of the He flow, $m/z = 42$ (e.g., $^{14}\text{N}^{14}\text{N}^{14}\text{N}$) and $m/z = 31$ (e.g., $^{15}\text{N}^{16}\text{O}$) were recorded to monitor the amount of air entrained in the interface tubing and ablation cell. After counts were stable and below 30,000 cps, the Ar nebulizer gas and He carrier gas flows were tuned to achieve $m/z = 248/232$ ratios of < 0.20 % (ThO/Th) and $m/z = 232/238$ ratios of 100 ± 1 % (Th/U), while ablating NIST 610 in line scan mode. Small amounts (3–4 ml/min) of high-purity (99.999 %) N_2 were admixed to the Ar nebulizer gas to increase the sensitivity. Once stable plasma conditions were reached, an automatic lens tune was performed on NIST 610 to maximize the sensitivity in the mid-mass range. Laser parameters for the tuning were 50 Hz repetition rate, 5 μm circular spot size, and 4 J/cm^2 fluence.

The single pulse response (SPR), i.e., the combined wash-in and wash-out, was monitored by ablating NIST 610 at 1 Hz and dosage 1 in line scan mode by recording $m/z = 238$ (U) with a dwell time of 5 ms. By averaging the peak shape of 300 single pulses, the SPR was determined and was between 80 ms (S2, S3) and 110 ms for S1 (full width at 10 % of the maximum intensity).

For mapping the elemental distribution within the target grains, mass channels $m/z = 34$ (S), $m/z = 55$ (Mn), $m/z = 57$ (Fe), $m/z = 72$ (Ge), and $m/z = 75$ (As) were recorded with dwell times of 20 ms for each element in session S1, and 2.5 ms for Mn, 1 ms for Fe, and 60 ms for As in sessions S2 and S3. Dwell times were optimized for a good signal-to-noise ratio and to avoid carry over of the aerosol beyond the laser spot diameter, which was between 2 and 3 μm . Applied dosages (degree of laser shot overlap) were between 10 and 20, repetition rates between 90 and 250 Hz, and scan speeds between 18 and 37.5 $\mu\text{m}/\text{s}$. Optimization of these parameters was based on obtaining a maximal spatial resolution and suppressing aliasing effects, while maintaining a signal/noise ratio of at least 20 for each mass channel. Depending on the size of the region of interest a single mapping took between 30 and 200 min.

Grains were mapped using a raster of unidirectional scans with no overlap between lines and a 2 s pause after each line to prevent memory effects. At regular intervals, typically every 30 min, a set of reference materials were ablated in 20–30 s long line scans using the same laser and ICP-MS parameters as for the mappings. MASS-1 (USGS) was used as the primary calibration standard and STDGL (fused glass containing sulfides RTS-4 and CZN-3; CODES Lab) and IMER5 (Ge-Ga-S

chalcogenide glass; University of Adelaide) as secondary standards. In each session, about 10–15 line scans of each reference material were recorded.

Raw data processing was performed using the software HDIP (Teledyne Photon machines). The background was corrected using a cubic spline function and a linear drift correction was performed using MASS-1. To obtain quantitative mappings, each pixel was calibrated on the MASS-1 line scans. In a second step, segments with Fe $> 100,000 \mu\text{g}/\text{g}$ and S $> 100,000 \mu\text{g}/\text{g}$ were defined in the mapped areas, to distinguish sulfides (pyrite, pyrrhotite) against siderite or the embedding medium (epoxy). To correct for differences in ablation yield between calibrant and sample, each pixel within such a segment was normalized to a sum of Fe + S = 100 wt %. Secondary reference materials were calibrated against MASS-1 and normalized using an internal standard (Fe for STDGL and S for IMER5).

Repeated line scans on the primary standard MASS-1 yielded an external precision (within session reproducibility) better than 4 % 2 RSE (RSE = relative standard error) for As. The internal precision based on a single line scan was better than 2.5 % 2 RSE. Concentrations of As obtained for IMER5 (reference value: 25.41 $\mu\text{g}/\text{g}$) were between 32.6 $\mu\text{g}/\text{g}$ – 34.1 $\mu\text{g}/\text{g}$ and for STDGL (reference value: $348 \pm 5.6 \mu\text{g}/\text{g}$) between 329.4 and 321.4 $\mu\text{g}/\text{g}$. The results for individual sessions overlap within the uncertainty and demonstrate good accuracy for As between 9 % (based on STDGL) and 35 % (based on IMER5). Deviations are attributed to varying matrix effects between the secondary reference materials (glasses) and MASS1 (pressed sulfide powder).

2.5. Analysis of quenched experimental and natural fluids

Arsenic concentrations in natural and synthetic fluids were measured using an Agilent 8900 ICP-MS/MS during four analytical sessions (S1–S4). All fluids were mixed online with a 0.5 $\mu\text{g}/\text{g}$ Ge solution that served as an internal standard to which all analyte counts were normalized. Samples were introduced into the Ar Plasma via a Micro Mist nebulizer and a Scott-type double-pass spray chamber. To reduce the plasma load, samples from sessions S1 and S2 (total dissolved solids, TDS, ~ 14.5 %) were diluted by a factor of 25 and samples from session S4 (TDS ~ 1.5 %) by a factor of 8 through online with Ar gas dilution using the Ultrahigh Matrix Introduction (UHMI) system of the Agilent 8900. The Äspö fluid was diluted offline by a factor of 10 using ultrapure H_2O (Rotipuran® Ultra). To avoid carry-over effects a two-step rinsing procedure was applied after every standard and sample using (1) 6 % HNO_3 and (2) 2 % HNO_3 each with a rinsing time of 30 s. Rinse solutions were prepared from diluting 65 % HNO_3 (Merck Suprapure®) with UP water. To establish the external calibration, a multi-element standard solution (Agilent environmental standard) was diluted with ultrapure water to achieve the desired calibration levels (see Table S2). Additionally, a commercial 5 % HNO_3 blank (Agilent) was used as the calibration blank. Accuracy was verified by measuring a second multi-element solution (LabKings quality control standard # 26) diluted to a concentration of 1 and 10 ng/g levels using ultrapure H_2O . The ICP-MS was operated in He-mode to avoid isobaric interferences of $^{40}\text{Ar}^{35}\text{Cl}^+$ on $^{75}\text{As}^+$. For each sample, 3–5 replicates were measured with ten mass sweeps per replicate and a dwell time of 0.5–2 ms for $m/z = 75$.

Measurement uncertainties correlate with As concentrations and vary from a few percent for high As contents up to a RSD of about 20 % at low As concentrations (Table 1). The highest measurement uncertainty for As was observed for the Äspö fluid sample (32 %, RSD, $n = 5$). Detection limits expressed as three times the standard deviation of the blank divided by the slope of the linear calibration regression are $< 1 \text{ ng}/\text{g}$ As (S1, S2, S4), with a minimum detection limit of 0.016 ng/g As in session S3 (Table S2). Accuracy is estimated to be better than 10 % based on the recovery of As from the quality check solution. The machine drift during each analytical session was < 10 %, as indicated by the recovery of the internal Ge standard from the HNO_3 blank solution.

2.6. Geochemical modeling

Geochemical modeling was performed using the PHREEQC software (Version 3.4.0), while species plots were generated using PhreePlot (Version 1). To ensure the accuracy of As stability data, we utilized the Nordstrom and Archer (2003) dataset as implemented in the wateq4f.dat database file. Thermodynamic data for all other chemical reactions were obtained from the Lawrence Livermore National Laboratory database (llnl.dat).

The model aimed to examine the impact of increasing As concentrations on As speciation. First, a solution was equilibrated with the atmosphere in a batch setup. Subsequently, all reactants (acetic acid, Na-acetate, thioacetamide and siderite) were added. The batch was then sealed and heated to 200°C, with the gas phase implemented at a volume 1.65 times that of the water phase to mimic the experimental vessel conditions. Finally, arsenic was incrementally added in 60 steps, with logarithmically equal steps covering the entire range of initial fluid As concentrations employed in the hydrothermal experiments, ranging from 0.001 mg/L to 100 mg/L. The input code of the model is accessible through the data repository at <https://doi.org/10.5281/zenodo.11086033>.

Species plots depicting arsenic speciation were generated using PhreePlot, employing a “hunt and track” approach with a resolution of 500. This approach provided a comprehensive understanding of the prevailing As species under the given pH and pressure conditions. The pH was set to the experimental pH of 4.9, while the pressure was set to 15 bar in alignment with the calculated pressure values obtained from the PHREEQC models. The x-axis and y-axis were chosen to fix the H₂S and O₂(gas) concentrations, respectively, enabling a specific investigation of the influence of these two parameters on As speciation. The plots showcased the dominant arsenic species, representing the species accounting for the largest number of moles of the main species. For example, if only two species were present, the species with a fraction greater than 50 % would be depicted as the dominant species.

3. Results

3.1. Texture and mineralogy of solid run products

Analysis by XRD, EPMA and micro-Raman showed that pyrite formed in all 21 experiments through replacement of siderite. Pyrite is consistently found at the outermost parts of the replaced siderite grains, while some siderite grains also display full replacement by pyrite (Fig. 1). In experiments with lower concentrations of the acetic acid buffer, the pyrite yield was highest with a mean phase content of 45 wt %. In these experiments, siderite is commonly fully replaced by pyrite (Fig. 1) and residual siderite is only detected in 3 out of 10 experiments (Table 1). Experiments conducted at higher buffer concentration have lower pyrite contents (mean = 28 wt %). Here, pyrite typically forms thin rims (10–100 µm) around relict siderite, which has been detected in all experiments at low buffer concentrations (Table 1). Pyrite occurs mainly in two configurations: as porous aggregates with occasional framboidal and lamellar habits and as dense anhedral to euhedral crystals (Fig. 1). The latter predominates at higher buffer concentrations, while at lower buffer concentrations, porous pyrite dominates. Euhedral pyrite up to ~40 µm in size was observed in the central part of fully replaced siderite and close to the siderite/pyrite interface in cases where siderite was only partially replaced (Fig. 1).

Marcasite is detected in 19 out of 21 experiments with contents ranging from 3 to 66 wt %. It is commonly overgrown by pyrite and its occurrence is restricted to the siderite/pyrite interface and the inner parts of fully replaced siderite. In the majority of the experiments, pyrite is the dominant FeS₂ polymorph. Other sulfides present in the run products are pyrrhotite (Fe_{1-x}S) in the high buffer experiments and greigite (Fe₃S₄) as well as mackinawite (FeS) in the low buffer experiments. While the presence of greigite and mackinawite is evident from

XRD, pyrrhotite has additionally been identified in reflected light, where it is overgrown by pyrite (Fig. 1). Magnetite and hematite were identified close to the siderite/pyrite interface, where magnetite forms an overgrowth on hematite and pyrite on magnetite and hematite (Fig. 1). Other minor phases detected by XRD are the Fe-sulfates melanterite (Fe (H₂O)₆SO₄·H₂O) and szomolnokite (FeSO₄·H₂O), arsenolite (As₂O₃) and quartz. Moreover, the run products of the experiments with high fluid As concentrations (100 µg/g), had a strikingly yellow-orange color, which is attributed to the presence of realgar. Its absence in the XRD data, is explained by the rapid light-induced decomposition of realgar to amorphous pararealgar (Pratesi and Zoppi, 2015).

3.2. Arsenic contents in pyrite close to the pyrite-fluid interface

The chemical analysis of pyrite is focused to the outermost regions of the replaced siderite, due to the complex textural and multiphase nature of the inner parts. To ensure high spatial resolution and sensitivity, the As concentrations in pyrite were determined by quantitative LA-ICP-MS mapping. The following data reduction strategy was employed. In a first step, transects with 7–25 pixels in width and perpendicular to the fluid-pyrite interface were inspected for their Fe/S ratio (wt. %). Only those transects were chosen, where Fe ≤ S, which indicated the presence of pyrite (S = 53.45 wt %, Fe = 46.55 wt %; Fe/S = 0.87). The mean sulfur concentrations of pyrite-assigned transects varied between 50–55 wt % (<https://doi.org/10.5281/zenodo.11086033>). Other Fe/S ratios with Fe > S are either attributed to pyrrhotite (Fe/S = 1.65), mackinawite (Fe/S = 1.74), greigite (Fe/S = 1.31) or a mixed analysis of pyrite + Fe-oxides and hence were discarded. Since marcasite and pyrite are indistinguishable by their Fe/S alone, we restricted the analyses to the first 30 µm of the replacement rim. This procedure largely avoids the analyses of marcasite, which is restricted to the more interior parts of the replacements rims (Fig. 1). Moreover, it facilitates the comparison between different experiments. From these regions, the As concentration across all pixels perpendicular to the transect is averaged at intervals of 3 µm intervals, equaling the image pixel size. As a result, 11 As concentration values were obtained for each transect, corresponding to the distance from the pyrite/fluid interface. The starting point for the quantification interval is selected to align with the moment when concentrations of both Fe and S initially reach a plateau (Fig. 2). This approach was adopted to mitigate potential biases arising from data acquisition and processing.

For the experimental pyrite, there are two main results. First, the As concentration decreases with distance to the pyrite/fluid interface, i.e., towards the relict siderite core (Figs. 2, 3a, Table 2). Occasionally, elongated As-hot spots were observed in the pyrite cores, that are aligned approximately parallel to the outer grain boundaries (Fig. 2f), but their As contents never exceeded those of the pyrite directly at the pyrite/bulk fluid interface. Secondly, the As contents in the pyrite rims systematically increase with increasing initial As contents in the experimental fluids (Figs. 2, 3a, Table 2). For instance, in experiments with an initial fluid As concentration of 0.001 µg/g, the mean As content of the pyrite rims ranged from 4.9 to 20.2 µg/g. In contrast, pyrite from fluids with 100 µg/g As exhibited As concentrations ranging from 18,239 to 60,695 µg/g (Table 2).

Moreover, the As concentration of three euhedral pyrite grains and two pyrite overgrowth on magnetite from Äspö (cf. Section 2.3) were determined by LA-ICP-MS mapping (Fig. 4). These display a mean As concentrations of 9.2 ± 5.9 µg/g (1 SD, n = 5) (Table 3). This is within the range of the As concentration of the synthetic pyrites from the experiments with the lowest initial As contents.

The comparison of As concentrations derived from randomly selected regions in pyrite by EPMA to the bulk compositions determined by LA-ICP-MS revealed a good correlation along a 1:1 regression line at concentrations >500 µg/g (Fig. S2). At lower As contents, the data of the two methods significantly deviate, which is due to the higher minimum detection limit of As in pyrite by EPMA (300 µg/g) compared to LA-ICP-

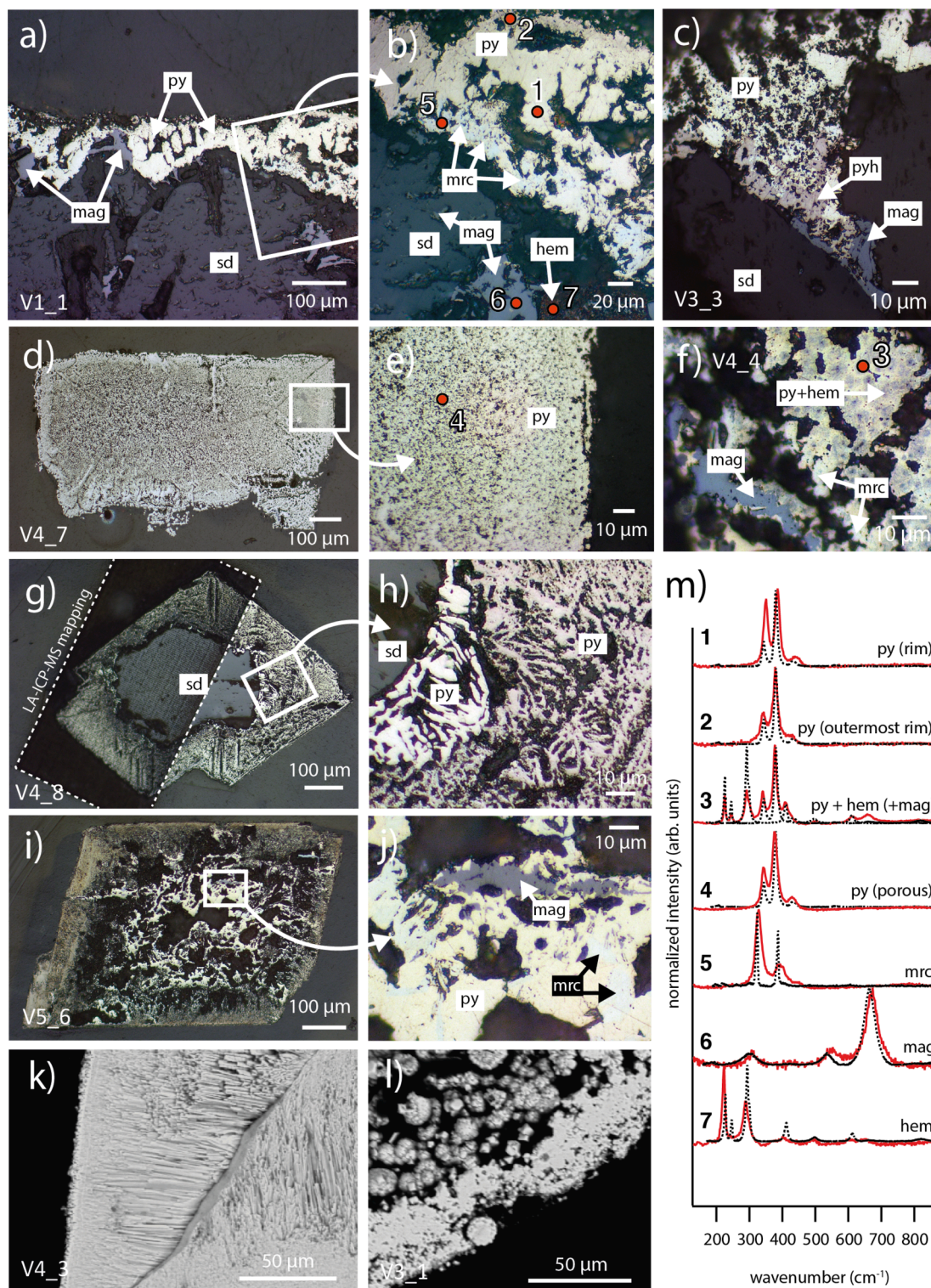


Fig. 1. Typical pyrite (py) textures in hydrothermal synthesis experiments. (a) Dense and thin pyrite rim forming at the former siderite (sd)/fluid interface in an experiment conducted at a high buffer concentration. At the pyrite/siderite interface, magnetite (mgt) is identified. (b) Close-up of the pyrite rim, additionally showing marcasite (mrc) close to the pyrite/siderite interface. Marcasite shows cream-white to bluish color in reflected light. Hematite (hem), red internal reflections is partly replaced by magnetite. (c) Pyrrhotite (pyh, brownish color) overgrowing magnetite and being overgrown by pyrite at the inner siderite interface (d) porous pyrite as typically observed in experiments conducted at lower buffer concentrations. (e) Close-up of the porous pyrite rim (f) pyrite replacing both magnetite and hematite close to the inner siderite interface. (g) Siderite grain displaying only partial replacement by pyrite. Here pyrite additionally forms lamellar crystal shapes. The dotted rectangle marks the region of interest as it appears after the LA-ICP-MS mapping. (h) Close-up of the lamellar pyrite habit appearing in experiments conducted at lower buffer concentrations. (i,j) Fully replaced siderite exhibiting the characteristic inner grain phase mixture comprising anhedral to euhedral pyrite overgrowing magnetite and marcasite. (k) Back scattered electron image of a porous lamellar pyrite rim (l) back scattered electron image of a porous framboidal pyrite rim m) Micro-Raman spectra collected from the run products to confirm the phase identification by reflected light. Numbers correspond to the analyses locations marked in the reflected light images in a-f. Black dotted lines are comparative spectra from the respective phases from the RRUFF database (see also <https://doi.org/10.5281/zenodo.11086033> for details). All Raman spectra are normalized to a main peak height of 1.

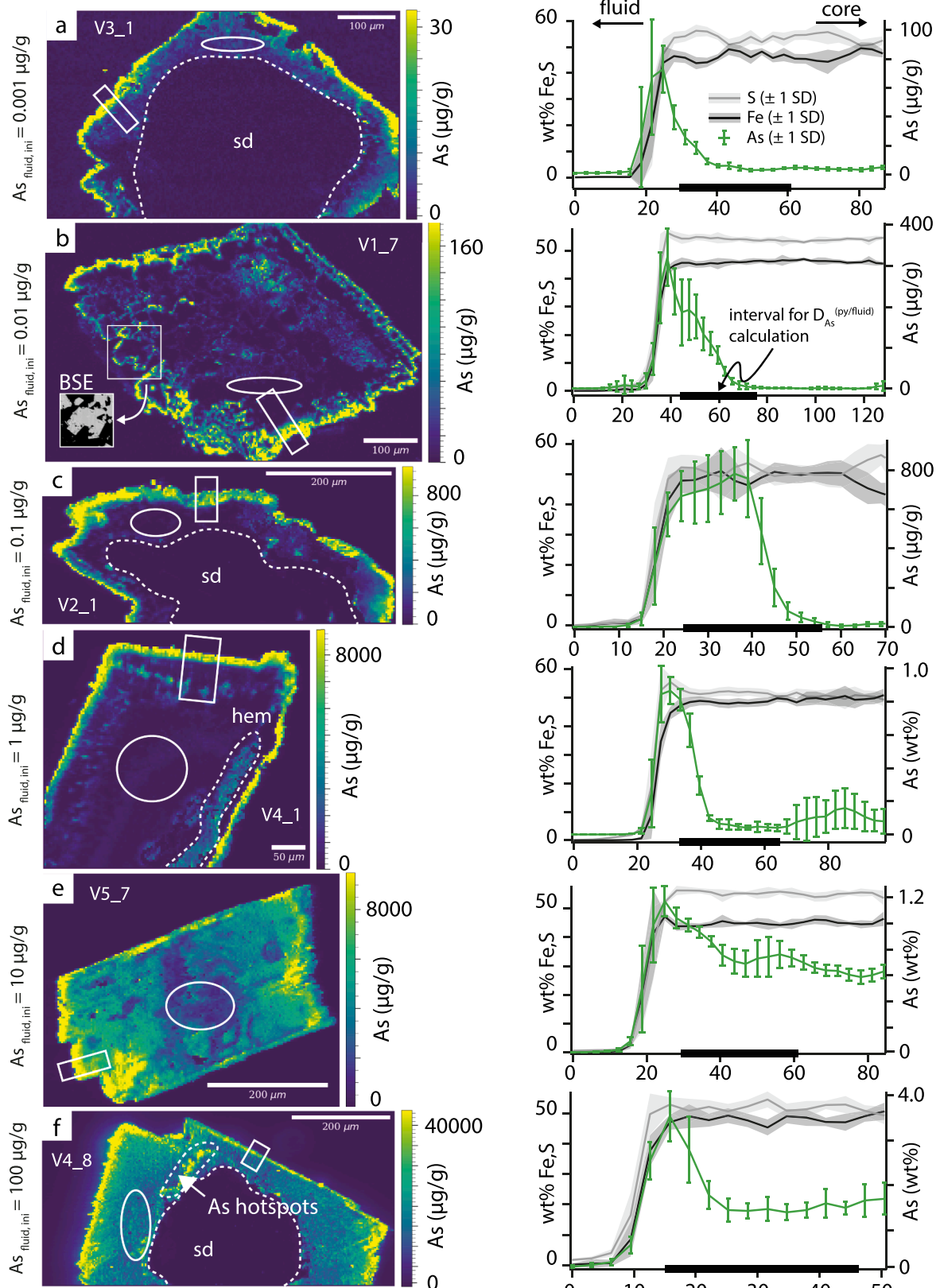


Fig. 2. LA-ICP-MS mappings of As concentrations in pyrite that forms during the replacement of siderite in hydrothermal experiments. For each envisaged initial fluid concentration one representative example is shown. An As gradient is observed throughout the experiments, with the highest values appearing in the outermost pyrite rims. The As concentration in pyrite increases with the As concentration of the fluids (mind the different scale for individual maps). For quantification of the As concentration in the pyrite rims, transects (white rectangles) have been extracted, which are displayed to the righthand side of each map. Only the first 30 µm after Fe and S have reached a plateau are considered. The As concentrations of the bulk phase assemblage of the innermost part of the replaced grains has been derived from averaging the pixel within the elliptical segments. For further information see Section 3.2. The image pixel size for all maps is 3 µm.

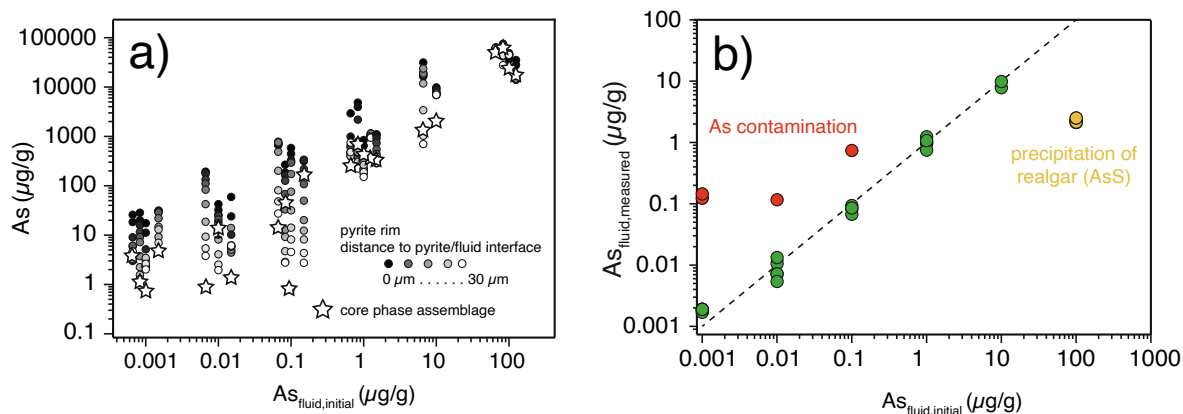


Fig. 3. (a) Arsenic concentrations in pyrite close to the pyrite/bulk fluid interface. Black and white colors denote the location within the transect across the pyrite rim, with black meaning closest to the pyrite/bulk fluid interface. Stars indicate the As concentrations of the bulk phase assemblage of the innermost part of the replaced grains. The locations of the rim transects and core segments is illustrated in Fig. 2 and in the data repository <https://doi.org/10.5281/zenodo.11086033>. (b) Plot of the As concentrations in the initial experimental fluid vs. As measured in the quenched experimental fluid. The experiments marked in green follow a 1:1 trend (dashed line) indicating no significant loss of arsenic or arsenic contamination. Yellow experiments suffer from As loss due to precipitation of realgar. Red experiments suffer from As-contamination and thus were not considered in this study. Fluid data for green and yellow experiments are compiled in Table 1.

MS (<1 µg/g at the single pixel level). Therefore, only the As contents derived from LA-ICP-MS analysis were considered for the data presentation and interpretation.

3.3. Arsenic concentration of the core phase assemblage

The inner core regions are composed of a phase mixture of mainly pyrite, marcasite, hematite and magnetite (Fig. 1). The intimate intergrowth of these minerals presents challenges for conducting analyses of As concentrations in individual phases by LA-ICP-MS. Instead, bulk As concentrations of the core phase assemblage have been determined by averaging As concentrations within elliptic segments assigned to the core regions of the replaced siderite grains (Fig. 2; <https://doi.org/10.5281/zenodo.11086033>). The results indicate that As concentrations at the innermost regions are about 1–2 orders of magnitude below the maximum As concentration measured at the pyrite rim (Fig. 3a, Table 2). Similar to the pyrite rims, we observe a general trend of decreasing As concentrations with decreasing As concentration in the initial fluid.

3.4. Arsenic concentrations in fluids

The As recovery from the synthetic fluids was determined by comparing the As contents of the initial fluid with those of the quenched fluid following pyrite synthesis (Fig. 3b). The results showed that the recovery of As ranged from 54 to 190 %, with an average recovery of approximately 85 %. Recoveries near 100 % indicate that pyrite growth and consecutive As incorporation did not change the As concentration of the bulk fluid, leading to similar As contents between the initial and quenched fluids. Conversely, recoveries >100 %, as observed in experiments with low initial As contents (0.001 µg/g) are attributed to minor As contamination at the 1 ng/g level likely originating from the siderite starting material (cf. Section 2.1, Fig. S1). In runs that were conducted in PTFE beakers previously used for fluids with 100 µg/g As, even higher levels of contamination of ~1 µg/g were observed (Fig. 3b). We attribute this type of As contamination to residual memory effects that remain despite of the thorough cleaning protocol for the PTFE beakers (cf. Section 2.2). These experiments were thus excluded from the present study, to avoid any impact of cross-contamination effects on the processed data. In the experimental runs V4_5 to V4_8, precipitation of realgar resulted in a significant loss of As, with recoveries ranging from only 2.1 % to 2.5 % (Fig. 3b).

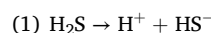
The natural groundwater samples from two separate boreholes

within the Äspö Hard-Rock-Laboratory (cf. Section 2.3) displayed low As concentrations of 0.3 and 0.4 ng/L (Table 3).

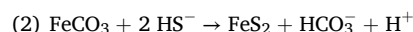
4. Discussion

4.1. Textural evolution and passivation during replacement of siderite by pyrite

The replacement of siderite follows an outward-to-inward progression, closely associated with pyrite formation through an interface-coupled dissolution-reprecipitation mechanism (Fig. 5). This connection is supported by the enduring rhombic siderite habit (Fig. 1g,i), which persists even in cases of complete siderite replacement by pyrite, suggesting an epitaxial relationship between the two phases (Putnis, 2014). As such, the siderite replacement proceeds via a two-step process, starting with the dissociation of H₂S via:



This is followed by coupled siderite dissolution and pyrite reprecipitation via:



Siderite replacement is not always complete, particularly not in experiments conducted at higher buffer concentrations (Fig. 1). This is attributed to the formation of pyrite acting as a passivating agent at the siderite/fluid interface. Similar observations were made during other dissolution-reprecipitation reactions, such as the weathering of wollastonite, feldspar and silicate glass (Nugent et al., 1998; Geisler et al., 2010; Ruiz-Agudo et al., 2016; Kutzschbach et al., 2018). Surface altered layers (SAL) were described in this context, that limit the fluid supply to the inner pristine mineral/glass – fluid interface, which usually results in a decrease of the dissolution rate. Depending on the porosity and thickness of the SAL, further dissolution is limited by volume diffusion through solid instead of fluid transport along connected pore space within the SAL. Hence, in the case of incomplete siderite replacement, it is expected that pyrite represents a passivating agent, with siderite dissolution being increasingly controlled by the supply and removal of S²⁻, H⁺ and HCO₃⁻ ions that can still penetrate the previously formed pyrite rim. In experiments with high buffer concentrations, the dominance of dense anhedral pyrite is observed early on (Fig. 1a), resulting in prompt passivation of the inner siderite/pyrite interface. Pyrrhotite,

Table 2

Arsenic concentrations of pyrite rims close the pyrite/bulk fluid interface and $D_{As}^{(py/fluid)}$ partitioning coefficients obtained from the hydrothermal synthesis experiments. Additionally, the As concentrations (± 1 SE, abs) of the core phase assemblage is presented.

Distance from pyrite-fluid interface (μm)	As ($\mu\text{g/g}$)	$D_{As}^{(py/fluid)}$	1 SE (%)	As ($\mu\text{g/g}$)	$D_{As}^{(py/fluid)}$	1 SE (%)	As ($\mu\text{g/g}$)	$D_{As}^{(py/fluid)}$	1 SE (%)	As ($\mu\text{g/g}$)	$D_{As}^{(py/fluid)}$	1 SE (%)
	V3_1	(As _{ini} = 0.001 $\mu\text{g/g}$)	(n = 13)	V3_1	(As _{ini} = 0.001 $\mu\text{g/g}$)	(n = 15)	V3_2	(As _{ini} = 0.001 $\mu\text{g/g}$)	(n = 12)	V3_3	(As _{ini} = 0.001 $\mu\text{g/g}$)	(n = 9)
0	25.8	25,830	5.2	28.4	28,431	15.2	17.5	17,515	6.4	30.1	30,125	27.2
3	18.4	18,438	6.0	20.1	20,077	8.2	11.2	11,202	7.0	30.1	30,055	12.7
6	9.0	9034	6.0	15.9	15,885	13.7	5.2	5157	8.8	31.6	31,585	10.3
9	5.9	5923	5.3	11.6	11,584	19.8	2.4	2407	8.1	30.5	30,522	9.0
12	6.1	6099	10.8	9.1	9141	23.9	2.3	2264	7.6	28.9	28,858	17.3
15	4.5	4509	11.3	7.2	7195	26.9	2.3	2270	10.1	22.0	21,953	17.5
18	3.0	2998	5.2	3.8	3753	29.6	2.4	2377	13.5	14.7	14,736	23.3
21	3.1	3150	3.1	2.2	2240	30.0	3.1	3066	9.8	9.2	9218	37.4
24	3.3	3322	3.8	1.6	1562	21.8	3.5	3456	4.3	13.0	13,027	85.1
27	4.2	4190	3.7	1.3	1288	10.0	2.6	2631	7.6	7.0	6998	83.0
30	4.7	4695	6.9	1.2	1152	9.5	2.0	2018	7.2	4.9	4889	92.2
Core	3.8 ± 0.2			1.1 ± 0.1			0.7 ± 0.1			4.9 ± 0.2		
	V1_5	(As _{ini} = 0.01 $\mu\text{g/g}$)	(n = 11)	V1_6	(As _{ini} = 0.01 $\mu\text{g/g}$)	(n = 16)	V1_7	(As _{ini} = 0.01 $\mu\text{g/g}$)	(n = 14)	V2_1	(As _{ini} = 0.1 $\mu\text{g/g}$)	(n = 11)
0	59.4	5942	7.2	42.4	4241	10.8	187	18,668	11.6	667	6667	5.8
3	24.0	2402	5.3	32.3	3230	7.1	193	19,342	10.2	687	6873	6.9
6	10.2	1024	4.6	26.0	2601	12.1	177	17,723	8.0	705	7055	7.3
9	6.2	621	6.8	24.7	2466	11.2	134	13,410	7.9	736	7358	6.6
12	4.8	479	11.1	20.8	2078	9.8	111	11,084	6.7	782	7821	5.3
15	4.4	443	12.1	17.7	1775	11.5	83.3	8331	6.7	757	7568	7.8
18	5.1	508	10.0	14.0	1396	12.8	42.5	4252	6.3	489	4889	10.5
21	5.8	585	10.6	8.2	815	10.0	18.6	1863	11.3	201	2014	14.3
24	6.0	596	12.8	4.1	408	10.8	9.3	931	29.1	81.0	810	16.5
27	5.9	587	12.0	2.5	252	11.0	5.4	539	32.4	48.3	483	15.4
30	6.1	612	9.7	2.0	195	6.7	3.8	379	22.1	27.5	275	19.9
Core	1.4 ± 0.1			13.8 ± 4.8			0.9 ± 0.1			14.6 ± 0.8		
	V2_2	(As _{ini} = 0.1 $\mu\text{g/g}$)	(n = 13)	V2_3	(As _{ini} = 0.1 $\mu\text{g/g}$)	(n = 15)	V2_5	(As _{ini} = 0.1 $\mu\text{g/g}$)	(n = 11)	V4_1	(As _{ini} = 1 $\mu\text{g/g}$)	(n = 17)
0	268	2677	10.2	584	5840	6.6	316	3162	8.0	2936	2936	4.5
3	186	1859	6.5	444	4444	9.1	326	3261	10.1	991	991	3.9
6	165	1653	4.5	332	3316	8.8	337	3375	17.7	647	647	10.9
9	126	1264	8.2	305	3052	8.0	218	2182	8.4	600	600	12.6
12	68.0	680	8.3	294	2942	14.4	108	1077	13.6	469	469	9.5
15	33.1	331	10.2	173	1728	13.7	49.8	498	24.0	401	401	6.9
18	12.9	129	18.6	75.9	759	11.9	20.2	202	28.4	476	476	15.7
21	9.2	92	39.7	31.9	319	11.4	12.3	123	23.3	434	434	11.9
24	4.7	47	38.3	14.2	142	12.6	8.2	82	23.3	399	399	11.4
27	2.9	29	23.3	8.2	82	13.2	4.3	43	20.8	480	480	21.9
30	2.8	28	11.4	4.6	46	13.0	2.7	27	26.1	751	751	33.2
Core	46.5 ± 2.4			0.8 ± 0.1			166 ± 1			255 ± 5		
	V4_2	(As _{ini} = 1 $\mu\text{g/g}$)	(n = 15)	V4_3	(As _{ini} = 1 $\mu\text{g/g}$)	(n = 19)	V4_4	(As _{ini} = 1 $\mu\text{g/g}$)	(n = 14)	V5_6	(As _{ini} = 1 $\mu\text{g/g}$)	(n = 19)
0	4843	4843	6.4	846	846	2.9	1054	1054	4.5	1107	1107	2.8
3	3962	3962	7.3	647	647	2.9	1157	1157	3.2	1061	1061	2.8
6	2192	2192	6.3	395	395	4.1	1055	1055	3.5	922	922	4.0
9	787	787	8.1	220	220	2.9	959	959	5.1	734	734	6.1
12	371	371	6.9	179	179	5.3	1001	1001	3.7	543	543	7.5
15	464	464	4.5	217	217	9.0	1004	1004	2.9	438	438	12.2
18	591	591	3.8	300	300	6.8	1094	1094	2.0	393	393	13.4
21	484	484	3.6	311	311	3.4	1129	1129	2.6	357	357	14.5
24	304	304	2.7	264	264	5.8	1032	1032	1.7	302	302	12.8
27	232	232	3.0	190	190	10.7	972	972	0.9	285	285	8.9
30	223	223	5.7	151	151	12.4	945	945	1.8	292	292	11.0
Core	685 ± 2.1			444 ± 9			360 ± 8			334 ± 6		
	V1_3	(As _{ini} = 10 $\mu\text{g/g}$)	(n = 20)	V5_7	(As _{ini} = 10 $\mu\text{g/g}$)	(n = 12)	V4_5	(As _{ini} = 100 $\mu\text{g/g}$)	(n = 25)	V4_6	(As _{ini} = 100 $\mu\text{g/g}$)	(n = 7)
0	31,496	3150	18.0	9866	987	1.5	62,117	621	3.0	57,983	580	2.9
3	16,426	1643	8.7	9332	933	1.3	59,474	595	2.3	65,850	658	2.7
6	16,946	1695	5.5	8612	861	1.3	61,216	612	2.9	75,440	754	2.1
9	19,324	1932	4.0	7557	756	3.0	59,252	593	3.7	69,352	694	2.3
12	18,006	1801	6.1	7099	710	4.0	54,805	548	2.4	61,873	619	3.6
15	18,862	1886	11.6	6894	689	4.2	59,223	592	1.6	51,316	513	6.1

(continued on next page)

Table 2 (continued)

Distance from pyrite-fluid interface (μm)	As ($\mu\text{g/g}$)	$D_{\text{As}}^{\text{(py/fluid)}}$	1 SE (%)	As ($\mu\text{g/g}$)	$D_{\text{As}}^{\text{(py/fluid)}}$	1 SE (%)	As ($\mu\text{g/g}$)	$D_{\text{As}}^{\text{(py/fluid)}}$	1 SE (%)	As ($\mu\text{g/g}$)	$D_{\text{As}}^{\text{(py/fluid)}}$	1 SE (%)
18	23,719	2372	5.6	7299	730	5.5	60,800	608	2.9	41,851	419	6.3
21	11,856	1186	3.9	7454	745	5.9	61,094	611	1.5	47,248	472	7.2
24	3401	340	11.6	7621	762	3.9	63,363	634	1.7	43,906	439	10.5
27	1032	103	15.9	7369	737	2.5	63,672	637	3.2	43,918	439	12.7
30	701	70	11.7	6987	699	2.3	62,626	626	3.1	27,759	278	11.7
Core	1373 \pm 23			2098 \pm 26			48948 \pm 382			63462 \pm 539		
	V4_7	(As _{ini} = 100 $\mu\text{g/g}$)	(n = 15)	V4_8	(As _{ini} = 100 $\mu\text{g/g}$)	(n = 12)						
0	36,146	361	3.9	35,264	353	4.5						
3	41,566	416	2.9	27,931	279	7.5						
6	44,536	445	2.7	17,776	178	5.0						
9	47,958	480	2.2	14,534	145	5.1						
12	48,769	488	1.3	14,330	143	3.5						
15	46,258	463	1.1	14,689	147	5.1						
18	46,033	460	0.9	14,031	140	3.6						
21	46,231	462	0.7	14,483	145	3.5						
24	47,169	472	1.4	15,991	160	5.7						
27	45,980	460	1.6	15,013	150	2.8						
30	45,001	450	0.9	16,593	166	6.2						
Core	24252 \pm 136											

n denotes the number of pixel that were averaged perpendicular to the concentration profile (see Fig. 2). SE denotes the standard error at the 1 s level (standard deviation divided by \sqrt{n}).

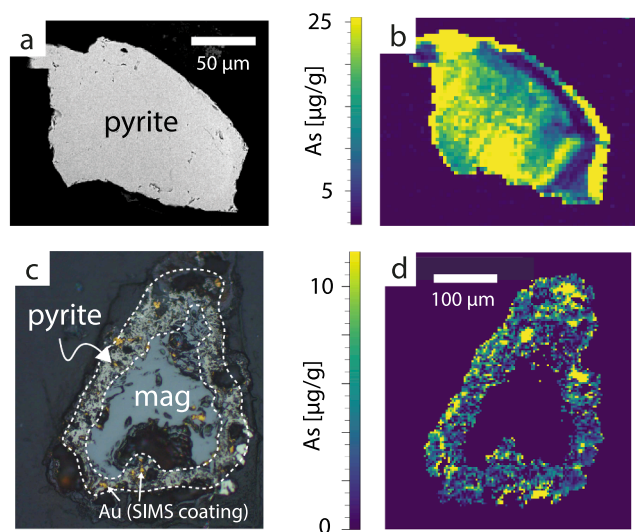


Fig. 4. Pyrite that formed in a borehole within the Äspö hard-rock laboratory over 17 years laboratory (see methods section). The BSE image in (a) shows a fragment of a euhedral dense pyrite crystal that displays elevated and zoned As concentrations as revealed by LA-ICP-MS mappings (b). Pyrite also occurs as porous overgrowth on magnetite and here also incorporates several $\mu\text{g/g}$ of As (d). Image pixel size is $3 \mu\text{m}$. The As concentration of the host fluid is between $0.3\text{--}0.4 \text{ ng/g}$. Gold particles are remnants from a gold coating required for SIMS analyses.

detected by XRD, is interpreted as an intermediate or precursor phase during pyrite formation, with subsequent overgrowth by pyrite (Fig. 1c), in accordance with previous studies (Schoonen & Barnes, 1991; Qian et al., 2011, Yao et al., 2021). Other pyrite precursor phases, such as mackinawite (Lennie and Vaughan, 1996; Rickard and Luther, 2007) and greigite (Schoonen and Barnes, 1991, Hunger and Benning, 2007), exclusively appear in experiments conducted at lower buffer concentrations (Table 1) and are considered as intermediate products during hydrothermal pyrite formation. We speculate that the nature of the precursor phase influences the crystal shape of the resulting pyrite. In experiments with low buffer concentrations, porous pyrite dominates,

Table 3

As concentrations and partition coefficients for natural pyrites and fluid from the Äspö hard-rock laboratory determined by (LA)-ICP-MS.

Pyrite crystal habit	Borehole	As ($\mu\text{g/g}$)		$D_{\text{As}}^{\text{(py/fluid)}}$
		Pyrite	Fluid	
Euhedral	KA3105 A:3	18.5	0.0003	61,667
Euhedral	KA3105 A:3	10.5		35,000
Euhedral	KA3105 A:3	2.8		9333
Porous on magnetite	KA3385 A:1	6.2	0.0004	15,500
porous on magnetite	KA3385 A:1	8.2		20,500
			mean	28,400
			1 SD	20,872

(1SE) for individual pyrite are better than 10 %. (1RSD) for fluid is 30 %.

facilitating ongoing migration of bulk fluid to the siderite/pyrite interface. Consequently, passivation is less effective compared to experiments with higher buffer concentrations, leading to the formation of larger cavities filled with inner fluid.

The consistent occurrence of marcasite is intriguing, as marcasite formation is typically associated with highly acidic $\text{pH} < 4$ (Qian et al., 2010, 2011). However, the sodium acetate acetic acid used in the hydrothermal experiments buffers at $\text{pH} = 4.89$, with the lower pH in quenched fluids being 4.35 (Table 1). The onset of marcasite formation at slightly higher $\text{pH} < 5$, as observed by Murowchick and Barnes (1986), provides a plausible explanation for marcasite formation. Moreover, Qian et al. (2011) highlighted the importance of the fluid saturation state with respect to pyrite/marcasite, indicating that marcasite is favored over pyrite in S^{2-} deficient solutions ($\text{SI} \ll 1000$). This situation is encountered close to the siderite/pyrite interface during earlier stages of the replacement reaction. In the immediate vicinity, the chemical composition of the so-called “inner fluid” is expected to deviate from that of the surrounding bulk fluid (Fig. 5). This is due to the passivating outer pyrite rim that limits the supply of H_2S -rich bulk fluid. Over time, the composition of the inner fluid transitions to the composition of the bulk fluid. This transformation is marked by the precipitation of pyrite as the stable FeS_2 polymorph, which is evident from the frequent observation of pyrite overgrowing marcasite in the core regions of the replaced siderite (Fig. 1b, j). Accordingly, the occurrence of

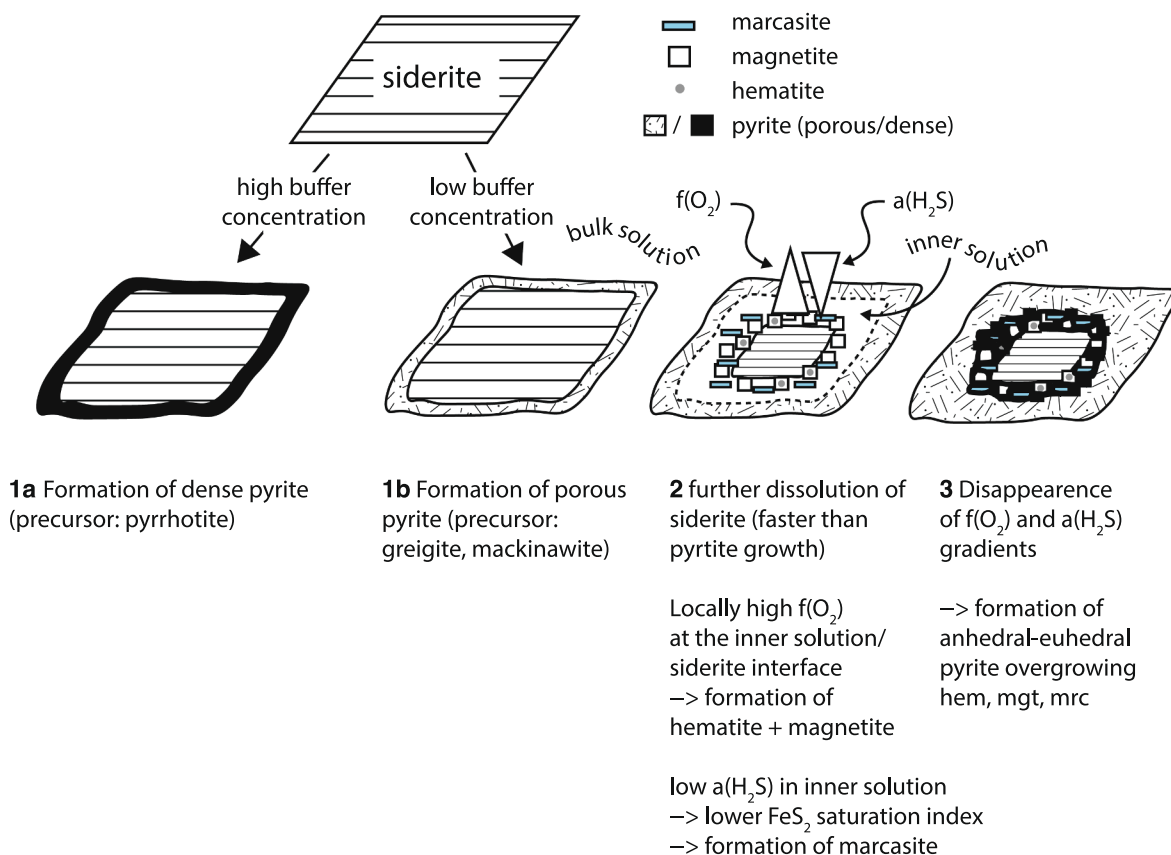


Fig. 5. Schematic drawing summarizing the most important observations with respect to the textural evolution during hydrothermal replacement of siderite by pyrite. For further information see Section 4.1.

hematite and magnetite at the siderite/inner fluid interface can be explained (Fig. 1c,f,i,j). Here, the high oxygen fugacity ($f(\text{O}_2)$) required for the formation of the Fe-oxides is maintained due to the limited interaction of inner fluid and bulk fluid. The occurrence of szomolnokite and melanterite is attributed to oxidation after opening of the beakers, where HS^- oxidizes to SO_4^{2-} , which eventually precipitates along with dissolved Fe^{2+} as melanterite or szomolnokite. A summary of the most important observations and conclusions regarding the textural evolution during siderite replacement by pyrite is presented in Fig. 5.

Pyrite with lamellar habit as observed in some experiments (Fig. 1g, h) is rather uncommon in nature. Rare natural analogue could be “feathery” or “wispy” pyrite habits observed in the Vatukoula epithermal Au-Ag-Te deposit, Fiji (Pals et al., 2003; Börner et al., 2021) and the Moonlight epithermal Au prospect, Queensland, Australia (Winderbaum et al., 2012). The exact crystallization mechanism of lamellar pyrite remains unclear, but crystal habits with high aspect ratios are known to be associated with precursor-mediated nucleation in hydrothermal synthesis experiments (Kutzschbach et al., 2016).

4.2. Nature of extreme As enrichment and zoning

A distinct feature of the pyrite products is the apparent zoning in As concentrations (Fig. 2). In general, we interpret the mechanism of As incorporation to involve a coupled adsorption/absorption process (Bostick and Fendorf, 2003; Han et al., 2013; Kusebauch et al., 2018). Thermodynamic modeling results demonstrate that the activity of As species exhibits variations depending on the fluid As concentration. At lower As concentrations, the thioarsenite species $\text{AsS}(\text{OH})(\text{HS})^-$ dominates, while $\text{As}_3\text{S}_4(\text{HS})_2^-$ becomes increasingly significant as As concentrations rise, eventually becoming the dominant species at As concentrations of 100 mg/L (Fig. 6). Similar to what has been inferred

for H_3AsO_3 and H_2AsO_3^- (Jörnsson and Sherman, 2008; Guo et al., 2011), it is expected that these thioarsenite species first adsorb onto the surface of siderite/pyrite. Subsequently, they become absorbed by newly forming pyrite through co-precipitation with iron (Fe) and sulfur (S) derived from thioacetamide breakdown and siderite dissolution (Bostick and Fendorf, 2003; Kusebauch et al., 2018). Changes in As speciation during individual experiments could potentially impact the incorporation and resulting As concentration in pyrite (Qian et al., 2013). However, mass balance calculations indicate that even a complete replacement of the siderite fraction (5 mg) would only lead to a change of approximately 0.03 log H_2S units, considering the high w/r ratios of 6000 encountered in the hydrothermal experiments. This shift is considered insignificant with respect to the As speciation in the fluid, regardless of the fluid As concentration (Fig. 6). Therefore, changes in the As speciation in the fluid during an experimental run do not influence the As zoning in the product pyrite. Nevertheless, it can be speculated that the pronounced As partitioning, particularly at lower As concentrations, may be associated with a potentially higher affinity of the $\text{AsS}(\text{OH})(\text{HS})^-$ species to the surfaces of siderite and/or pyrite, in contrast to $\text{As}_3\text{S}_4(\text{HS})_2^-$, which becomes increasingly dominant as fluid As concentrations decrease.

In a recent study, Xing et al. (2019) introduced a mechanism of As incorporation into pyrite through prolonged exposure to As-bearing fluids. The study showed that the interaction between pyrite and a basalt-buffered fluid with an As concentration of 20 $\mu\text{g/g}$, can increase the As contents in pyrite by an order of magnitude from 0.6 to 5.7 wt %. The authors ascribe this to a remobilization and reprecipitation process, which is increasingly efficient at higher fluid/rock ratios. While the highest fluid/rock ratio in Xing et al. (2019) is 120, the fluid/rock ratios in our experiments are even higher (~6000). Thus a similar self-enrichment mechanism may steer the observed extreme As

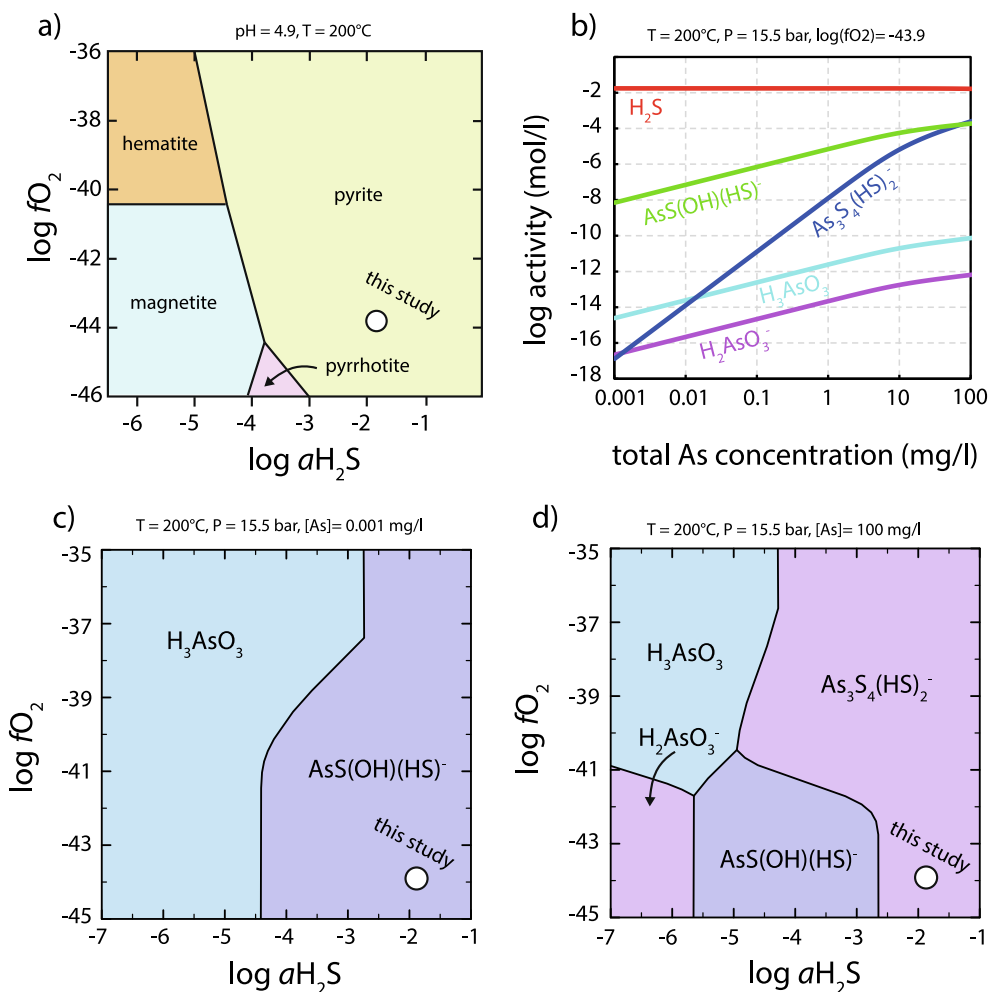


Fig. 6. (a) Dominant solid phases as a function of oxygen fugacity and H_2S activity under As free conditions demonstrating that pyrite is the stable phase in the hydrothermal experimental system. Due to the high w/r ratio of 6000, the change in H_2S activity due to pyrite formation is insignificant. (b) Dominant aqueous arsenic species at the experimental oxygen fugacity ($\log f\text{O}_2 = -43.9$) and temperature ($T = 200^\circ\text{C}$) as a function of arsenic concentration. The range of fluid As concentrations resembles the range investigated in this study. At lower As concentration the thioarsenite species AsS(OH)(HS)^- dominates, while $\text{As}_3\text{S}_4(\text{HS})_2^-$ becomes progressively more significant as As concentrations increase, ultimately becoming the dominant species at As concentrations of 100 mg/l. Predominance regions of all stable aqueous species as a function of oxygen fugacity and H_2S activity for lowest and highest As concentrations are presented in c) and d). Predominance regions for all As concentrations are accessible via the supplementary material (Fig. S3). Details of the PHREEQC model are presented in the methods section and the input code can be accessed through the data repository <https://doi.org/10.5281/zenodo.11086033>.

partitioning from the fluid into in the rim domains of the pyrite products in our experimental study (Fig. 2). Early forming pyrite thus is expected to have low initial As contents, which increases over time by continuous interaction with the surrounding large fluid reservoir. Consequently, early-formed pyrite experiences a larger time-integrated fluid/solid ratio, than pyrite that formed later. In analogy to the findings by Xing et al. (2019), this would lead to higher As concentrations in early pyrite compared to late pyrite, corresponding to the As zoning between the rim and core domains in pyrite from our experiments (Fig. 2).

In nature, the formation of porous (i.e., framboidal, lamellar) pyrite is commonly related to fast nucleation rates induced by strong physicochemical gradients (e.g., temperature), whereas euhedral pyrite typically precipitates at more stable fluid conditions. Moreover, framboidal pyrite is often associated with microbial processes (e.g. Widodo et al., 2010; Beck et al., 2011). Natural euhedral pyrite is often found to be depleted in various trace elements compared to coexisting porous pyrite (Deditius et al., 2011; Meng et al., 2020; Grant et al., 2018; Román et al., 2019; Falkenberg et al., 2021; Börner et al., 2021). This is in line with the observations in our study (Fig. 2b) and the results obtained by Prokofiev et al. (2022), who observed that coarsening during pyrite recrystallization in synthesis experiments resulted in decreasing

As contents in pyrite. Hence, we conclude that the As enrichment at the rim compared to the core of the synthetic pyrites, was enhanced by fast nucleation rates at disequilibrium conditions during early and rapid formation of porous pyrite as opposed to euhedral and dense pyrite. Alternatively, the As depleted core domains could be explained by the pyrite rim that acted as a filter adsorbing most of the As from the experimental fluid, which limited the amount of As available at the siderite-pyrite interface (Fig. 5). We note that the aforementioned processes are not mutually exclusive and might act together to produce the observed extreme As enrichment and As gradients in the product pyrites of our experiments. The elongated As-hot spots that are occasionally found in the pyrite cores (Fig. 2f) are interpreted to result from early pyrite formation along open cleavage planes in the siderite starting material (Fig. S1).

4.3. As partitioning in low versus high As fluids

The precipitation of pyrite or any other phase did not significantly impact the As concentration of the bulk fluid. This conclusion is supported by the high overall recovery of As from the quenched fluid, facilitated by employing a high fluid-to-solid ratio (~6000).

Consequently, we calculated pyrite-fluid partitioning coefficients ($D_{As}^{py/fluid}$) using the As concentration of the initial experimental fluid ($As_{fluid, initial}$) and the As concentrations measured in pyrite close to the pyrite/fluid interface (Fig. 7, Table 2). The innermost part of the replaced siderite grains is not considered for calculating partitioning coefficients for any of the present minerals. This due to (1) The multiphase and intertwined nature of the innermost phase assemblage hinders the accurate determination of As concentrations in individual phases with certainty and (2) the chemistry of the inner fluid likely differs from the bulk experimental fluid. This is evidenced by the occurrence of marcasite, which we ascribed to a lower SI compared to the bulk fluid (see Section 4.1). Similar to the anticipated S^{2-} deficiency in the inner solution, it is expected that the As concentrations are lower compared to those in the bulk solution. However, the exact As concentration of the inner fluid remains unknown.

Currently, data for $D_{As}^{py/fluid}$ values in reduced hydrothermal systems (e.g. $\log fO_2 = -43.9$, Fig. 6) are limited to fluids with relatively high As contents of 1–100 $\mu\text{g/g}$ (Fig. 8), to which we refer as the high-As range in the following. Our study confirms previous findings within the high-As range ($>1 \mu\text{g/g}$ $As_{fluid, initial}$), where most $D_{As}^{py/fluid}$ values is <2000 (Figs. 7 and 8, Table 2; Reich et al., 2005; Su et al., 2008, 2009, 2012; Qian et al., 2013; Large et al., 2016; Kusebauch et al., 2018). This is true also for experiments with an initial As concentration of 100 $\mu\text{g/g}$. In these experiments, realgar was identified as an additional byproduct (cf. Section 3.1). We conclude due to the good agreement of our and previously published $D_{As}^{py/fluid}$ values (Fig. 8), that realgar forms as a quench phase after the experimental runs during cooling (cf. Section 2.1) and does not affect the As budget and partitioning during the experimental runs. In addition, an increase in the $D_{As}^{py/fluid}$ values is observed in the high-As range with decreasing initial As fluid contents, particularly with respect to the outermost parts of the pyrite rims (Fig. 7). This trend agrees with previous results from hydrothermal experiments conducted at pH 4.7 and 5.8 (Fig. 8; Kusebauch et al., 2018).

In fluids with initial As contents $<1 \mu\text{g/g}$, the $D_{As}^{py/fluid}$ values further increase until reaching a maximum value of ~ 30000 in experiments with the lowest As concentrations of 0.001 $\mu\text{g/g}$ As in the initial experimental fluids. These values are at least an order of magnitude higher than the $D_{As}^{py/fluid}$ values of the high-As fluids ($\geq 1 \mu\text{g/g}$) from the same pyrite domain. It is crucial to acknowledge that the computed $D_{As}^{py/fluid}$ values for the inner parts of the pyrite rims should be interpreted as minimum values. This is because the pyrite/siderite interfacial fluid likely had lower As contents compared to the surrounding bulk fluid, which we relate to As-scavenging by the early forming pyrite rims (cf.

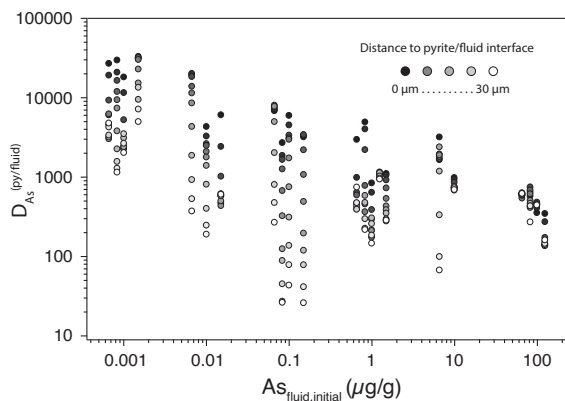


Fig. 7. As partitioning coefficients D_{As} calculated from the As concentration in pyrite divided by the As concentration in the initial fluid. Only LA-ICP-MS data are shown. Black and white colors denote the location within the transect across the pyrite rim, with black meaning closest to the pyrite/bulk fluid interface. Note (1) the increasing partitioning of As into pyrite with decreasing As concentrations in the fluid and (2) the decreasing D_{As} with increasing distancing to the pyrite/bulk fluid interface. Data are compiled in Table 2.

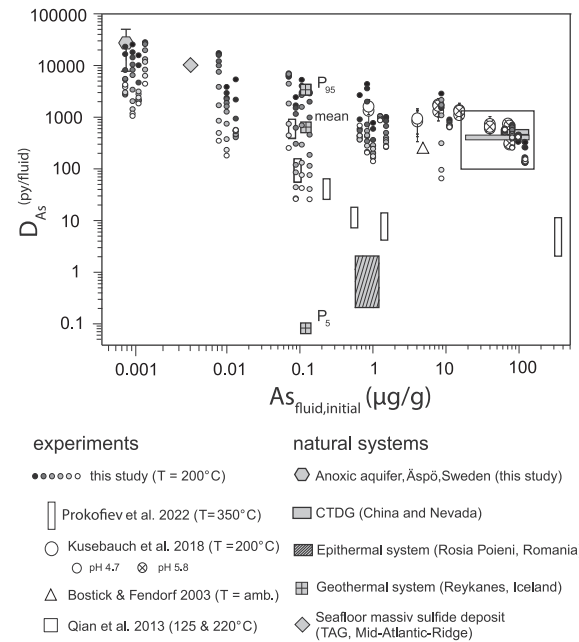


Fig. 8. Comparison of $D_{As}^{py/fluid}$ values obtained in this study to other experimental studies and natural systems. Data of Kusebauch et al., 2019, Qian et al., 2013 and Prokofiev are from replacement experiments using siderite, magnetite and FeS/FeOHHS as precursor phases. Results from Bostick and Fendorf (2003) are from sorption experiments. Data for natural Carlin type gold deposits (CTDG) are from two localities in China (Su et al., 2008; Su et al., 2009, Su et al., 2012) and Nevada (Large et al., 2016; Reich et al., 2005). Data for geothermal systems are from Libbey and Williams-Jones (2016) and Hardardóttir et al. (2009) who studied fluids and pyrites from the Reykjanes geothermal system in Iceland. Data for the seafloor massive sulfide are from an actively forming hydrothermal mound on the TAG segment of Mid-Atlantic ridge Grant et al. (2018). Here the mean value and the 5th and 95th percentile are shown. The epithermal system is represented by epithermal veins at the Rosia-Poieni porphyry Cu-Au deposit in Romania (Kouzmanov et al., 2010, Deditius et al., 2014). Tabulated data is available from the data repository <https://doi.org/10.5281/zenodo.11086033>.

Section 4.2).

A similar trend of increasing $D_{As}^{py/fluid}$ values is displayed by the data presented by Prokofiev et al. (2022), which however exhibit an overall shift towards lower $D_{As}^{py/fluid}$ values at a given fluid As concentration (Fig. 8). This is attributed to the different experimental (cf. Section 2.1) set up of Prokofiev et al. (2022), where FeS (i.e., pyrrhotite) or FeOHHS were replaced by pyrite at elevated fluid temperatures of 350°C. This is important, as As preferentially partitions into the fluid relative to pyrite at higher temperatures (Xing et al., 2019), which explains the overall lower $D_{As}^{py/fluid}$ compared to our experimental runs.

Experiments with fluid As concentrations ranging from 1 to 100 $\mu\text{g/g}$ were conducted at lower buffer concentrations, resulting in the predominant formation of porous pyrite. Conversely, experiments with fluid As concentrations below 1 $\mu\text{g/g}$ were performed at higher buffer concentrations, leading to the formation of dense pyrite. These differing pyrite morphologies could introduce additional effects on the determined empirical $D_{As}^{py/fluid}$ values. Kusebauch et al. (2019) observed that in experiments where both porous and dense euhedral pyrite formed, the As concentration in euhedral pyrite was approximately 1.2–2.5 times higher than in porous pyrite (see their Fig. 6). This disparity was attributed to the non-equilibrium conditions of rapid replacement reactions that form porous pyrite, as opposed to the slower growth of dense euhedral pyrite under partially equilibrated conditions. Interestingly, this general observation aligns with the As concentrations found in the Äspö pyrite, where, on average, euhedral pyrite contains about 1.5 times more As compared to porous pyrite (Table 3). However, our $D_{As}^{py/fluid}$

fluid) values determined for porous pyrite at fluid As concentrations between 1 and 100 $\mu\text{g/g}$ are in good agreement with previously published data (Fig. 8), in particular with the results of Kusebauch et al., 2019, whose partitioning coefficients were exclusively based on dense euhedral pyrite. Even if we consider a 2.5-fold increase in the $D_{\text{As}}^{\text{(py/fluid)}}$ for fluid As concentrations between 1 and 100 $\mu\text{g/g}$, the trend of increasing $D_{\text{As}}^{\text{(py/fluid)}}$ with decreasing fluid As concentrations remains evident. The $D_{\text{As}}^{\text{(py/fluid)}}$ values for fluid As concentrations of 0.001 $\mu\text{g/g}$ exceed those for fluid As concentrations of 100 $\mu\text{g/g}$ by an order of magnitude, up to a factor of approximately 50 (Table 2).

4.4. Comparison with natural systems and implications

4.4.1. Groundwater

The formation of stable arsenopyrite-like surface layers (FeAsS) due to As adsorption on pyrite and siderite is described as an effective mechanism for mitigating As contaminations under reducing conditions in groundwater (Bostick and Fendorf, 2003; Bostick et al., 2004; Jörnsson and Sherman, 2008). This is confirmed by experiments performed by Bulut et al. (2014), who achieved a reduction of As concentration in the fluid by up to 99 % due to As adsorption on fine-grained pyrite. The initial As concentration in the fluids investigated by the aforementioned studies was between ~ 4 $\mu\text{g/g}$ (Bostick et al., 2004) and 10 $\mu\text{g/g}$ (Bulut et al., 2014), which also lies in the As range of our experimental fluids. Our extremely high $D_{\text{As}}^{\text{(py/fluid)}}$ values (up to $\sim 30,000$, Table 2) for low-As fluids (<1 $\mu\text{g/g}$) demonstrate that As adsorption on pyrite is also effective in less contaminated fluids that display As concentrations in the ng/g to $\mu\text{g/g}$ range. This is underlined by the Äspö pyrite that shows bulk As concentrations between 2.8 and 18.5 $\mu\text{g/g}$, despite its formation from fluids with very low As contents of only 0.0003–0.0004 $\mu\text{g/g}$ (Table 3). Interestingly, the formation of the Äspö pyrite is related to microbial activity that provides H_2S from SO_4^{2-} reduction (Drake et al., 2015; Yu et al., 2019; Pidchenko et al., 2023) and bio-enhanced As trapping by pyrite has already been successfully tested as a technically feasible strategy for groundwater remediation at an industrial site in Florida (Saunders et al., 2018). Saunders et al. (2018) showed that the As content of a fluid can be reduced from 0.3–0.5 $\mu\text{g/g}$ to 0.05 $\mu\text{g/g}$ within a few weeks by precipitation of pyrite.

To assess the effect of $D_{\text{As}}^{\text{(py/fluid)}}$ on the As sequestration potential, we calculated the As decrease in a 1 ng/g As fluid as a function of the fluid

mass, based on the formation of 100 mg of pyrite (Fig. 9; Table S4). The results show that for 1 l of water (fluid/solid ratio = 10,000) and at a $D_{\text{As}}^{\text{(py/fluid)}}$ value of 30,000, the As concentration in the fluid would experience a decrease of ~ 75 % to 0.25 ng/g. By contrast, previously published $D_{\text{As}}^{\text{(py/fluid)}}$ values that are in the range of 100–1000 (Fig. 8) would result in decrease of As concentration in the fluid of only 1–10 %. This calculation demonstrates the potential of siderite replacement in effectively scavenging As from groundwater into the pyrite structure, in addition to adsorption on the pyrite surface. Such information plays a critical role in designing (cost) efficient remediation strategies.

4.4.2. Hydrothermal systems

The comparison of our experimental $D_{\text{As}}^{\text{(py/fluid)}}$ values with those derived from natural hydrothermal systems by coupled pyrite-fluid analysis yielded comparable, but also strongly diverging results (Fig. 8). The $D_{\text{As}}^{\text{(py/fluid)}}$ values from Äspö (this study) and from the actively forming TAG seafloor massive sulfide deposit at the Mid-Atlantic Ridge (Grant et al., 2018) are representative for natural (hydrothermal) systems with low-As fluids (<1 $\mu\text{g/g}$) and are in perfect agreement with our experimentally derived results (Fig. 8). Similarly, $D_{\text{As}}^{\text{(py/fluid)}}$ values for natural Carlin-type systems (Su et al., 2008, 2009, 2012; Large et al., 2016; Reich et al., 2005) are representative for high-As fluids (>1 $\mu\text{g/g}$) and also agree with our $D_{\text{As}}^{\text{(py/fluid)}}$ values and those that were previously published. Importantly, the pyrite formation temperatures of Äspö (~ 14 °C; Drake et al., 2015), TAG (300–350 °C; Grant et al., 2018), Carlin-type systems (180–220 °C, Su et al., 2012) and our experimental approach (200 °C) cover a wide range applicable to various natural systems. The comparable $D_{\text{As}}^{\text{(py/fluid)}}$ values of our experimental study and these natural systems therefore suggest that fluid temperature is only a subordinate effect on the As fluid-pyrite partitioning. Xing et al. (2019), argue that As preferentially partitions into the fluid at higher temperatures. However, their results strictly apply to equilibrium conditions. In our study, As incorporation is more likely to be kinetically controlled. Based on our data, particularly in these non-equilibrium scenarios, which encompass the majority of the lower temperature natural systems, it becomes evident that the primary factor governing As partitioning into pyrite is the concentration of As in the fluid. This finding agrees with the data presented by Prokofiev et al. (2022), where increasing $D_{\text{As}}^{\text{(py/fluid)}}$ values are observed with decreasing fluid As content (Fig. 8, Section 4.3). However, the discrepancy between the $D_{\text{As}}^{\text{(py/fluid)}}$ values from the high-temperature experiments ($T = 350$ °C) conducted by Prokofiev et al. (2022) and our own at $T = 200$ °C suggests that temperature and fluid concentration effects may as well be superimposed (see Fig. 8).

While the calculated mean $D_{\text{As}}^{\text{(py/fluid)}}$ for the active Reykjanes geothermal system on Iceland align with our experimental data within the specified As concentration of the fluid (0.11–0.15 $\mu\text{g/g}$; Hardardóttir et al., 2009), it is important to note that the Reykjanes data exhibits a considerable variability, that surpasses the range observed in our study (Fig. 8). The Reykjanes geothermal system is actively boiling (Hardardóttir et al., 2009), which typically results in the preferential partitioning of As into the vapour phase (Pokrovski et al., 2002, 2013). Importantly, Libbey and Williams-Jones (2016) showed that the trace element composition of pyrite from the Reykjanes geothermal system varies in response to fluid boiling, as known from many other geothermal and epithermal systems, and which typically results in strong compositional variations in pyrite chemistry (Román et al., 2019; Nestmeyer et al., 2021; Börner et al., 2021; Grosche et al., 2023). The values of $D_{\text{As}}^{\text{(py/fluid)}}$ derived from our experiments under non-boiling fluid conditions should thus be applied with caution to boiling hydrothermal systems.

In addition, the competitive incorporation of As between co-genetic hydrothermal minerals can also strongly control the final As budget of pyrite, and as a result the related $D_{\text{As}}^{\text{(py/fluid)}}$ values. While pyrite is the most important host for As in Carlin-type ores (Deditius et al., 2014) and seafloor massive sulfides at mid-ocean ridges, such as TAG (Keith et al.,

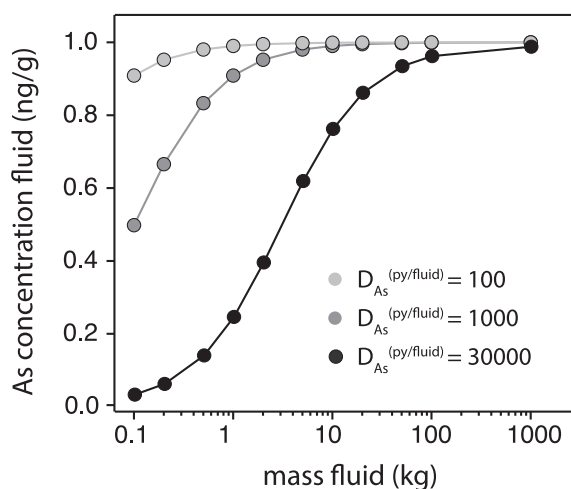


Fig. 9. Calculation of the decrease of the As concentration in a fluid with an initial As concentration of 1 ng/g after formation of 100 mg of pyrite as a function of the total fluid mass assuming a Rayleigh fractionation process. The $D_{\text{As}}^{\text{(py/fluid)}}$ of 30,000 represents the maximum partitioning coefficient observed in this study for fluid with a low As concentration of 1 ng/g. Detailed results of the modeling are tabulated in Table S4 and the data repository available at <https://doi.org/10.5281/zenodo.11086033>.

2016; Grant et al., 2018), hydrothermal systems related to other geological settings (e.g., epithermal, porphyry) commonly host various As-bearing minerals (e.g., enargite, luzonite, tennantite-tetrahedrite, loellingite) that may compete with pyrite regarding the As incorporation (Einaudi et al., 2003; Simmons et al., 2005; Hedenquist et al., 2017; Falkenberg et al., 2022). The Rosia Poieni porphyry Cu deposit in Romania, which features an epithermal overprint, is such an example. Here, enargite may suppress the As incorporation into pyrite leading to the comparatively low $D_{As}^{(py/fluid)}$ values (Fig. 8; Kouzmanov et al., 2010; Deditius et al., 2014).

The high $D_{As}^{(py/fluid)}$ values reported in this study imply that pyrite originating from As-poor fluids likely is highly As-enriched, which challenges whether elevated As contents in natural pyrite are generally linked to an As-rich fluid phase. For instance, the $D_{As}^{(py/fluid)}$ values of the high-As fluid range ($>1 \mu\text{g/g}$) would yield a fluid As content of 0.024–0.130 $\mu\text{g/g}$ for a pyrite with 40 $\mu\text{g/g}$ As. By contrast, our new $D_{As}^{(py/fluid)}$ values for the low-As range ($<1 \mu\text{g/g}$) demonstrate that fluid As contents could have been in a much lower range of only 0.001–0.005 $\mu\text{g/g}$.

5. Summary and conclusions

Our study demonstrates that the fluid-pyrite As partitioning is highly sensitive to the initial fluid As content, which is particularly true for the low-As range ($<1 \mu\text{g/g}$), as indicated by strongly increasing $D_{As}^{(py/fluid)}$ values (up to 30,000) with decreasing fluid As concentrations. The resulting strong As enrichment in pyrite can be attributed to a complex interplay of nucleation rate, exposure time of pyrite to the experimental fluid, the fluid flow regime towards the fluid-siderite interface and sorption phenomena at the siderite/pyrite surfaces.

Importantly, our $D_{As}^{(py/fluid)}$ values surpass previously published data on pyrite-fluid partitioning, which has significant implications for natural systems. For instance, our results suggest that the replacement of siderite by pyrite through a coupled dissolution reprecipitation reaction may serve as an efficient process for groundwater remediation, even in less severely contaminated aquifers. Hence, a better understanding of the dynamics of fluid-pyrite interaction may help to develop more effective strategies for managing and remediating As contamination in groundwater. The applicability of our new $D_{As}^{(py/fluid)}$ values also extends to natural hydrothermal systems operating at higher temperatures (up to 200 °C). Here, our findings reveals that the $D_{As}^{(py/fluid)}$ values are predominantly controlled by the initial As concentration of the fluid and superimpose potential temperature effects. Hence, our new $D_{As}^{(py/fluid)}$ values provide a valuable tool for a more reliable reconstruction of the fluid As concentrations based on pyrite chemistry, which enables a more precise prediction of the behavior and fate of As in low-As (ng/g- $\mu\text{g/g}$) fluid environments.

Finally, our study highlights the effectiveness of quantitative LA-ICP-MS mapping in providing precise and accurate elemental distributions in geomaterials even at the micrometer scale. This analytical approach provides valuable insights into the mechanisms that govern fluid-rock interaction, contributing to a better understanding of fluid-related geochemical processes in general.

Data availability

Data are available through Zenodo at <https://doi.org/10.5281/zenodo.11086033>.

Declaration of Generative AI and AI-assisted technologies in the writing process

During the preparation of this work the author(s) used ChatGPT (OpenAI) in order to improve spelling and readability. After using this tool, the author(s) reviewed and edited the content as needed and take full responsibility for the content of the publication.

CRedit authorship contribution statement

Martin Kutzschbach: Writing – review & editing, Writing – original draft, Visualization, Supervision, Project administration, Methodology, Investigation, Data curation, Conceptualization. **Frederik Dunkel:** Writing – review & editing, Investigation. **Christof Kusebauch:** Writing – review & editing, Methodology, Investigation, Conceptualization. **Ferry Schiperski:** . **Frederik Börner:** Writing – review & editing, Investigation. **Henrik Drake:** Writing – review & editing, Resources, Investigation. **Kevin Klimm:** Writing – review & editing, Investigation. **Manuel Keith:** Writing – review & editing, Writing – original draft, Project administration, Funding acquisition, Conceptualization.

Declaration of competing interest

The authors declare that they have no known competing financial interests or personal relationships that could have appeared to influence the work reported in this paper.

Acknowledgments

We acknowledge Paul Böttcher and Cordelia Lange for assistance during the hydrothermal experiments, XRD analyses and sample preparation, as well as Nico Müller for preparing the polished epoxy mounts. This study was financially supported by a DFG grant (KE 2395/1-1) to Manuel Keith and grants of the Swedish Research Council (contracts 2021-04365), Formas (contract 2020-01577), J. Gust. Richert foundation (contract 2023-00850), the Crafoord Foundation (contract 20210524) awarded to Henrik Drake. We thank Johannes Giebel for providing the Ivigtut siderite from the mineral collection of the TU Berlin and Benjamin Wade for providing the IMER5 reference material. Also we acknowledge the Swedish Nuclear Fuel and Waste for providing access to the Äspö fluid samples. Finally, we thank Prof. Thomas Neumann for the opportunity to work at the MAGMA Lab of the Technische Universität Berlin.

Appendix A. Supplementary material

The supplementary material contains major and trace element composition of starting siderite from Ivigtut (Table S1), the figures of merit for As-fluid analyses by LA-ICP-MS/MS (Table S2), the results of the EPMA analyses of pyrite from all hydrothermal experiments (Table S3), and the results of the geochemical modeling of the As concentration in fluids (Table S4). Additionally, it contains reflected light images and trace element mappings of starting siderite (Fig. S1), the correlation of As concentrations by EPMA and LA-ICP-MS (Fig. S2), and predominance regions of As species for all investigated fluid As concentrations generated using PhreePlot (Version 1), Fig. S3. Supplementary material to this article can be found online at <https://doi.org/10.1016/j.gca.2024.05.027>.

References

- Baraño, D., Boente, C., Rodríguez-Valdés, E., Fernández-Braña, A., Jiménez, A., Gallego, J.L.R., González-Fernández, B., 2020. Arsenic release from pyrite ash waste over an active hydrogeological system and its effects on water quality. *Environ. Sci. Pollut. Res.* 27, 10672–10684.
- Beck, M., Riedel, T., Graue, J., Köster, J., Kowalski, N., Wu, C., Wegener, G., Lipsewers, Y., Freund, H., Böttcher, M., Brumsack, H.-J., Cypionka, H., Rullkötter, J., Engelen, B., 2011. Imprint of past and present environmental conditions on microbiology and biogeochemistry of coastal Quaternary sediments. *Biogeosciences* 8, 55–68.
- Blanchard, M., Alfredsson, M., Brodholt, J., Wright, K., Catlow, C.R.A., 2007. Arsenic incorporation into FeS₂ pyrite and its influence on dissolution: a DFT study. *Geochim. Cosmochim. Acta* 71, 624–630.
- Börner, F., Keith, M., Smith, D.J., Barry, T.L., Neumann, T., Klemd, R., 2021. Fingerprinting fluid evolution by trace elements in epithermal pyrite, Vatukola Au-Te deposit, Fiji. *Ore Geol. Rev.* 137, 104314.
- Bostick, B.C., Fendorf, S., 2003. Arsenite sorption on troilite (FeS) and pyrite (FeS₂). *Geochim. Cosmochim. Acta* 67, 909–921.

- Bostick, B.C., Chen, C., Fendorf, S., 2004. Arsenite retention mechanisms with estuarine sediments of Pescadero, CA. *Environ. Sci. Technol.* 38, 3299–3304.
- Bulut, G., Yenial, Ü., Emiroglu, E., Sirkeci, A.A., 2014. Arsenic removal from aqueous solution using pyrite. *J. Clean. Prod.* 84, 526–532.
- Burnside, N.M., Banks, D.B., Boyce, A.J., 2016. Sustainability of thermal energy production at the flooded mine workings of the former Caphouse Colliery, Yorkshire, United Kingdom. *Int. J. Coal Geol.* 164, 85–91.
- Ciobanu, C.L., Cook, N.J., Utsunomiya, S., Kogagwa, M., Green, L., Gilbert, S., Wade, B., 2012. Gold-telluride nanoparticles revealed in arsenic-free pyrite. *Am. Mineral.* 97, 1515–1518.
- Craig, J.R., Vokes, F.M., Solberg, T.N., 1998. Pyrite: physical and chemical textures. *Miner. Deposita* 34, 82–101.
- Deditius, A.P., Reich, M., Kesler, S.E., Utsunomiya, S., Chryssoulis, S.L., Walshe, J., Ewing, R.C., 2014. The coupled geochemistry of Au and As pyrite from hydrothermal ore deposits. *Geochim. Cosmochim. Acta* 140, 644–670.
- Deditius, A.A., Utsunomiya, S., Renock, D., Ewing, R.C., Ramana, C.V., Becker, U., Kesler, S.E., 2008. A proposed new type of arsenian pyrite: composition, nanostructure and geological significance. *Geochim. Cosmochim. Acta* 72, 2919–2933.
- Deditius, A.P., Utsunomiya, S., Reich, M., Kesler, S.E., Ewing, R.C., Hough, R., Walshe, J., 2011. Trace metal nanoparticles in pyrite. *Ore Geol. Rev.* 42, 32–46.
- Drake, H., Tullborg, E.-L., Whitehouse, M., Sandberg, B., Blomfeldt, Astrom, M.E., 2015. Extreme fractionation and micro-scale variation of isotopes during bacterial sulphate reduction in deep groundwater systems. *Geochim. Cosmochim. Acta* 161, 1–18.
- Einaudi, M.T., Hedenquist, J.W., Inan, E.E., 2003. Sulfidation state of fluids in active and extinct hydrothermal systems: transitions from porphyry to epithermal environments. *Spec. Publ. – Soc. Econ. Geol.* 10, 285–314.
- Evangelou, V.P., 1995. Pyrite Oxidation and Its Control. CRC Press, Boca Raton, p. 292.
- Falkenberg, J.J., Keith, M., Haase, K.M., Bach, W., Klemm, R., Strauss, H., Yeo, I.A., Rubin, K.H., Storch, B., Anderson, M.O., 2021. Effects of fluid boiling on Au and volatile element enrichment in submarine arc-related hydrothermal systems. *Geochim. Cosmochim. Acta* 307, 105–132.
- Falkenberg, J.J., Keith, M., Haase, K.M., Sporer, C., Bach, W., Klemm, R., Strauss, H., Storch, B., Peters, C., Rubin, K.H., Anderson, M.O., 2022. Spatial variations in magmatic volatile influx and fluid boiling in the submarine hydrothermal systems of Niutahi Caldera, Tonga Rear-Arc. *Geochim. Geophys. Geosyst.* 23, e2021GC010259.
- Flude, S., Haschke, M., Storey, M., 2017. Application of benchtop micro-XRF to geological material. *Mineral. Mag.* 81, 923–948.
- Geisler, T., Janssen, A., Schreiter, D., Stephan, T., Berndt, J., Putnis, A., 2010. Aqueous corrosion of borosilicate glass under acidic conditions: a new corrosion mechanism. *J. Non Cryst. Solids* 356, 1458–1465.
- Grant, H.L.J., Hannington, M.D., Petersen, S., Frische, M., Fuchs, S.H., 2018. Constraints on the behavior of trace elements in the actively-forming TAG deposit, Mid-Atlantic Ridge, based on LA-ICP-MS analyses of pyrite. *Chem. Geol.* 498, 45–71.
- Grosche, A., Klemm, R., Denkel, K., Keith, M., Haase, K.M., Voudouris, P.C., Alfieri, D., Wiedenbeck, M., 2023. Sources, transport, and deposition of metal(loid)s recorded by sulfide and rock geochemistry: constraints from a vertical profile through the epithermal Profitis Ilias Au prospect, Milos Island, Greece. *Miner. Deposita* 58, 1101–1122.
- Guo, H., Li, Y., Zhao, K., Ren, Y., Wei, C., 2011. Removal of arsenite from water by synthetic siderite: behaviours and mechanisms. *J. Hazard. Mater.* 186, 1847–1854.
- Han, D.S., Song, J.K., Batchelor, B., Abdel-Wahab, A., 2013. Removal of arsenite (As(III)) and arsenate (As(V)) by synthetic pyrite (FeS₂): synthesis, effect of contact time, and sorption/desorption envelopes. *J. Colloid Interface Sci.* 392, 311–318.
- Hardardóttir, V., Brown, K.L., Fridriksson, Th., Hedenquist, J.W., Hannington, N.D., Thorhallsson, S., 2009. Metals in deep liquid of the Reykjanes geothermal system, southwest Iceland: implications for the composition of seafloor black smoker fluids. *Geology* 37, 1103–1106.
- Hedenquist, J.W., Arribas, R.A., Aoki, M., 2017. Zonation of sulfate and sulfide minerals and isotopic composition in the far southeast porphyry and leptano epithermal Cu-Au deposits, Philippines. *Resour. Geol.* 67, 174–196.
- Hunger, S., Benning, L.G., 2007. Greigite: a true intermediate on the polysulfide pathway to pyrite. *Geochem. Trans.* 8, 1.
- Jones, G.W., Pichler, T., 2003. Relationship between pyrite stability and arsenic mobility during aquifer storage and recovery in Southwest Florida. *Sci. Total Environ.* 41, 723–730.
- Jörnsson, J., Sherman, D.M., 2008. Sorption of As (III) and As (V) to siderite, green rust (fougerite) and magnetite: implications for arsenic release in anoxic groundwaters. *Chem. Geol.* 255, 173–181.
- Keith, M., Häckel, F., Haase, K.M., Schwarz-Schampera, U., Klemm, R., 2016. Trace element systematics of pyrite from hydrothermal vents. *Ore Geol. Rev.* 72, 728–745.
- Keith, M., Smith, D.J., Jenkin, G.R.T., Holwell, D.A., Dye, M.D., 2018. A review of Te and Se systematics in hydrothermal pyrite from precious metal deposits: insights into ore-forming processes. *Ore Geol. Rev.* 96, 269–282.
- Kouzmanov, K., Pettke, T., Heinrich, C.A., 2010. Direct analysis of ore-precipitating fluids: combined IR microscopy and LA-ICP-MS study of fluid inclusions in opaque ore minerals. *Econ. Geol.* 105, 351–373.
- Kusebauch, C., Oelze, M., Gleeson, S., 2018. Partitioning of arsenic between hydrothermal fluids and pyrite during experimental siderite replacement. *Chem. Geol.* 500, 136–147.
- Kusebauch, C., Gleeson, S.A., Oelze, M., 2019. Coupled partitioning of Au and As into pyrite controls formation of giant Au deposits. *Sci. Adv.* 5, eaav5891.
- Kutzschbach, M., Wunder, B., Rhede, D., Koch-Müller, M., Ertl, A., Gierster, G., Heinrich, W., Franz, G., 2016. Tetrahedral boron in natural and synthetic HP/UHP tourmaline: Evidence from Raman spectroscopy, EMPA, and single-crystal XRD. *Am. Mineral.* 101, 93–104.
- Kutzschbach, M., Guttman, P., Marquardt, K., Werner, S., Henzler, K.D., Wilke, M., 2018. A transmission X-ray microscopy and NEXAFS approach for studying corroded silicate glasses at the nanometer scale. *Phys. Chem. Glasses-Eur. J. Glass Sci. Technol. Part B* 59, 11–26.
- Large, S.J.E., Bakker, E.Y.N., Weis, P., Wälle, M., Ressel, M., Heinrich, C.A., 2016. Trace elements in fluid inclusions of sediment-hosted gold deposits indicate a magmatic-hydrothermal origin of the Carlin ore trend. *Geology* 44, 1015–1018.
- Large, R.R., Danyushevsky, L., Hollit, C., Maslennikov, V., Meffre, S., Gilbert, S., Foster, J., 2009. Gold and trace element zonation in pyrite using a laser imaging technique: implications for the timing of gold in orogenic and Carlin-type sediment-hosted deposits. *Econ. Geol.* 104, 635–668.
- Lennie, A.R., Vaughan, D.H., 1996. Spectroscopic studies of iron sulfide formation and phase relation at low temperatures. *Mineral Spectroscopy: A Tribute to Roger G. Burns. MW Schaefer*, pp. 117–156.
- Libbey, R.B., Williams-Jones, A.E., 2016. Relating sulfide mineral zonation and trace element chemistry to subsurface processes in the Reykjanes geothermal system, Iceland. *J. Volcanol. Geoth. Res.* 310, 225–241.
- Meng, X., Li, X., Chu, F., Zhu, J., Lei, J., Li, Z., Wang, H., Chen, L., Zhu, Z., 2020. Trace element and sulfur isotope compositions for pyrite across the mineralization zones of a sulfide chimney from the East Pacific Rise (1–2°S). *Ore Geol. Rev.* 116, 103209.
- Mukherjee, I., Large, R.R., 2016. Pyrite trace element chemistry of the Valkerri Formation, Roper Group, McArthur Basin: evidence for atmospheric oxygenation during the Boring Billion. *Precamb. Res.* 281, 13–26.
- Murovchick, J.B., Barnes, H.L., 1986. Marcasite precipitation from hydrothermal solutions. *Geochim. Cosmochim. Acta* 50, 2615–2629.
- Nestmeyer, M., Keith, M., Haase, K., Klemm, R., Voudouris, P., Schwarz-Schampera, U., Strauss, H., Kati, M., Mugganas, A., 2021. Trace element signatures in pyrite and marcasite from Shallow Marine Island Arc-related hydrothermal vents, calypso vents, New Zealand, and Paleochori Bay, Greece. *Front. Earth Sci.* 9, 641654.
- Nordstrom, D.K., Archer, D.G., 2003. Arsenic thermodynamic data and environmental geochemistry. In: Welch, A.H., Stollenwerk, K.G. (Eds.), *Arsenic in Ground Water*. Springer, Boston, MA.
- Nordstrom, D.K., 1982. Aqueous pyrite oxidation and the consequent formation of secondary iron minerals. In: Kittrick, J.A., Fanning, D.S., Hosser, L.R. (Eds.), *Acid Sulfate Weathering*, Vol. 17. Soil Science Society of America Special Publication, pp. 37–56.
- Nugent, M.A., Brantley, S.L., Pantano, C.G., Maurice, P.A., 1998. The influence of natural mineral coatings on feldspar weathering. *Nature* 295, 588–591.
- Oliveira, M.L., Ward, C.R., Izquierdo, M., Sampaio, C.H., de Brum, I.A., Kautzmann, R. M., Silva, L.F., 2012. Chemical composition and minerals in pyrite ash of an abandoned sulphuric acid production plant. *Sci. Total Environ.* 430, 34–47.
- Palenik, C.S., Utsunomiya, S., Reich, M., Kesler, S.E., Wang, L., Ewing, R.C., 2004. “Invisible” gold revealed: direct imaging of gold nanoparticles in a Carlin-type deposit. *Am. Mineral.* 89, 1359–1366.
- Pals, D.W., Spry, P.G., Chryssoulis, S., 2003. Invisible gold and tellurium in arsenic-rich pyrite from the Emperor gold deposit, Fiji: implications for gold distribution and deposition. *Econ. Geol.* 98, 479–493.
- Pidchenko, I., Christensen, J.N., Kutzschbach, M., Ignatyev, K., Puigdomenesch, I., Tullborg, E.-L., Roberts, N.M.W., Rasbury, E.T., Northrup, P., Tappero, R., Kvashnina, K.O., Schäfer, T., Suzuki, Y., Drake, H., 2023. Deep anoxic aquifers could act as sinks for uranium through microbial-assisted mineral trapping. *Commun. Earth Environ.* 4, 128.
- Pokrovski, G.S., Zakirov, I.V., Roux, J., Testemale, D., Hazemann, J.-L., Bychlov, A.Y.U., Golikova, G.V., 2002. Experimental study of arsenic speciation in vapor phase to 500 °C: implications for As transport and fractionation in low-density crustal fluids and volcanic gases. *Geochim. Cosmochim. Acta* 66, 3453–3480.
- Pokrovski, G.S., Borisova, A.Y., Bychkov, A.Y., 2013. Speciation and transport of metals and metalloids in geologic vapors. *Rev. Mineral. Geochem.* 76, 165–218.
- Pokrovski, G.S., Kokh, M.A., Proux, O., Hazemann, J.-L., Bazarkina, E.F., Testemale, D., Escoda, C., Boiron, M.-C., Blanchard, M., Aigouy, T., Gouy, A., Parseval, P., Thibaut, M., 2019. The nature and partitioning of invisible gold in the pyrite-fluid system. *Ore Geol. Rev.* 109, 545–563.
- Pokrovski, G.S., Escoda, C., Blanchard, M., Testemale, D., Hazemann, J.-L., Gouy, S., Kokh, M.A., Boiron, M.-C., de Parseval, F., Aigouy, T., Menjot, L., de Parseval, P., Proux, O., Rovezzi, M., Béziat, D., Salvi, S., Kouzmanov, K., Bartsch, T., Pöttgen, R., Doert, T., 2021. An Arsenic driven pump for invisible gold in hydrothermal systems. *Geochem. Perspect. Lett.* 17, 39–44.
- Pratesi, G., Zoppi, M., 2015. An insight into the inverse transformation of realgar altered by light. *Am. Mineral.* 100, 1222–1229.
- Prokofiev, V.Y., Tagirov, B.R., Brovchenko, V.D., Reukov, V.L., Filiminova, O.N., Zorina, L.D., Abramova, V.D., Kovalchuk, E.V., Mezhueva, A.A., Nikolaeva, I.Y., Tarnopolskaya, M.E., Akinfiev, N.N., Kransov, A.N., Komarov, V.B., Bortnikov, N.S., 2022. Gold in natural and synthetic pyrite: a case of the Darasung Gold District, Eastern, Transbaikal Region, Russia. *Geol. Ore Deposits* 64, 329–349.
- Putnis, A., 2014. Why mineral interfaces matter. *Science* 343, 1441–1442.
- Qian, G., Brugger, J., Skinner, W.M., Chen, G.R., Pring, A., 2010. An experimental study of the mechanism of the replacement of magnetite by pyrite up to 300 °C. *Geochim. Cosmochim. Acta* 74, 5610–5630.
- Qian, G., Xia, F., Brugger, J., Skinner, W.M., Bei, J., Chen, G., Pring, A., 2011. Replacement of pyrrhotite by pyrite and marcasite under hydrothermal conditions up to 220 °C: an experimental study of reaction textures and mechanisms. *Am. Mineral.* 96, 1878–1893.

- Qian, G., Brugger, J., Testemale, D., Skinner, W., Pring, A., 2013. Formation of As (II)-pyrite during experimental replacement of magnetite under hydrothermal conditions. *Geochim. Cosmochim. Acta* 100, 1–10.
- Reich, M., Becker, U., 2006. First-principles calculations of the thermodynamic mixing properties of arsenic incorporation into pyrite and marcasite. *Chem. Geol.* 225, 278–290.
- Reich, M., Kesler, S.E., Utsunomiya, S., Palenik, C.S., Chryssoulis, S.L., Ewing, R.C., 2005. Solubility of gold in arsenian pyrite. *Geochim. Cosmochim. Acta* 69, 2781–2796.
- Reich, M., Deditius, A.P., Chryssoulis, S., Li, J.W., Ma, C.Q., Parada, M.A., Mittermayr, F., 2013. Pyrite as a record of hydrothermal fluid evolution in a porphyry copper system: a SIMS/EMPA trace element study. *Geochim. Cosmochim. Acta* 104, 42–62.
- Rickard, D., Luther, G.W., 2007. Chemistry of iron sulfides. *Chem. Rev.* 107, 514–562.
- Román, N., Reich, M., Leisen, M., Morata, D., Barra, F., Deditius, A.P., 2019. Geochemical and micro-textural fingerprints of boiling in pyrite. *Geochim. Cosmochim. Acta* 246, 60–85.
- Ruiz-Agudo, E., King, H.E., Patiño-López, L.D., Putnis, C.V., Geisler, T., Rodriguez-Navarro, C., Putnis, A., 2016. Control of silicate weathering by interface-coupled dissolution-precipitation processes at the mineral-solution interface. *Geology* 44, 567–570.
- Saunders, J.A., Lee, M.-K., Dhakal, P., Ghandehari, S.S., Wilson, T., Billor, M.Z., Uddin, 2018. Bioremediation of arsenic-contaminated groundwater by sequestration of arsenic in biogenic pyrite. *Appl. Geochem.* 96, 233–243.
- Savage, K.S., Tingle, T.N., O'Day, P.A., Waychunas, G.A., Bird, D.K., 2000. Arsenic speciation in pyrite and secondary weathering phases, Mother Lode gold district, Tuolumne County, California. *Appl. Geochem.* 15 (1219), 1244.
- Schmidt, K., Schönberg, D.-G., Hannington, M.D., Anderson, M.O., Bühring, B., Haase, K., Haruel, C., Lupton, J., Koschinsky, A., 2017. Boiling vapour-type fluids from the Nifonea vent field (New Hebrides Back-Arc, Vanuatu, SW Pacific): geochemistry of an early-stage, post-eruptive hydrothermal system. *Geochim. Cosmochim. Acta* 207, 185–209.
- Schoonen, M.A.A., Barnes, H.L., 1991. Mechanisms of pyrite and marcasite formation from solution: III. Hydrothermal processes. *Geochim. Cosmochim. Acta* 55, 3491–3501.
- Simmons, S.F., White, N.C., John, D.A., 2005. Geological characteristics of epithermal precious and base metal deposits. Special Publication – Society of Economic Geologists. Simon, G., Huang, H., Penner-Hahn, J.E., Kesler, S.E., and Kao, L.S. (1999) Oxidation state of gold and arsenic in gold-bearing arsenian pyrite. *Am. Mineral.* 84, 1071–1079.
- Sliwinski, M.G., Maicej, G., Kitajima, K., Spicuzza, M.J., Orland, I.J., Ishida, A., Fournelle, J.H., Valley, J.W., 2018. SIMS bias on isotope ratios in Ca-Mg-Fe carbonates (Part II): $\delta^{18}\text{O}$ and $\delta^{13}\text{C}$ matrix effects along the magnesite-siderite solid-solution series. *Geostand. Geoanal. Res.* 42, 49–76.
- Smith, A.H., Smith, M.M.H., 2004. Arsenic drinking water regulations in developing countries with extensive exposure. *Toxicology* 198, 39–44.
- Stuyfzand, P.J., Bonte, M., 2023. A critical review of arsenic occurrence, fate and transport in natural and modified groundwater systems in The Netherlands. *Appl. Geochem.* 150, 105596.
- Su, W., Heinrich, C.A., Pettke, T., Zhang, X., Hu, R., Xia, B., 2009. Sediment-hosted gold deposits in Guizhou, China: products of wall-rock sulfidation by deep crustal fluids. *Econ. Geol.* 104, 73–93.
- Su, W.C., Xia, B., Zhan, H.T., Zhang, X.C., Hu, R.Z., 2008. Visible gold in arsenian pyrite at the Shuiyindong Carlin-type gold deposit, Guizhou, China: implications for the environment and processes of ore formation. *Ore Geol. Rev.* 33 (667), 679.
- Su, W., Zhang, H., Hu, R., Ge, X., Xia, B., Chen, Y., Zhu, C., 2012. Mineralogy and geochemistry of gold-bearing arsenian pyrite from the Shuiyindong Carlin-type gold deposit, Guizhou, China: implications for gold depositional processes. *Miner. Deposita* 47, 653–662.
- Widodo, S., Oschmann, W., Bechtel, A., Sachsenhofer, R.F., Anggayana, K., Puetmann, W., 2010. Distribution of sulfur and pyrite in coal seams from Kutai Basin (East Kalimantan, Indonesia): implications for paleoenvironmental conditions. *Int. J. Coal Geol.* 81, 151–162.
- Winderbaum, L., Ciobanu, C.L., Cook, N.J., Paul, M., Metcalfe, A., Gilbert, S., 2012. Multivariate analysis of an LA-ICP-MS trace element dataset for pyrite. *Math. Geosci.* 44, 823–842.
- Xing, Y., Brugger, J., Tomkins, A., Sharov, Y., 2019. Arsenic evolution as a tool for understanding formation of pyrite gold ores. *Geology* 47, 335–338.
- Yao, X., Xia, F., Brugger, J., Kartal, M., Adegoke, I.A., 2021. Rapid marcasite to pyrite transformation in acidic low-temperature hydrothermal fluids and saturation index control on FeS_2 precipitation dynamics and phase selection. *ACS Earth Space Chem.* 5, 2453–2465.
- Yu, C., Drake, H., Lopez-Fernandez, M., Whitehouse, M., Dopson, M., Åström, M.E., 2019. Micro-scale isotopic variability of low-temperature pyrite in fractured crystalline bedrock – a large Fe isotope fractionation between $\text{Fe(II)}_{\text{aq}}$ /pyrite and absence of Fe-S isotope co-variation. *Chem. Geol.* 522, 192–207.